Damage caused by Tropical Cyclone Pat, Cook Islands, February 2010.
Photo: National Environment Service, Government of the Cook Islands

# Chapter 7
# Projections Based on Downscaling

# Summary

- Downscaled projections are provided that complement, but do not replace, the projections discussed in Chapter 6.
- The Conformal Cubic Atmospheric Model (CCAM) 60 km downscaled projections for the Pacific Climate Change Science Program region are broadly consistent with those of the global climate models presented in Chapter 6. However, some differences between these and the CCAM projections are noted, such as bands of rainfall decrease around latitudes 8°N and 8°S. These projections are also supported by the additional downscaling results using a variety of other regional climate models.
- The CCAM 8 km downscaled projections show regional-scale variations of the climate change signal, largely related to the topography of Partner Countries.
- Statistical downscaling shows slightly less warming, more consistent with the observed trends.
- Tropical cyclone frequency in the PCCSP region is likely to decrease by the late 21st century. There is a moderate level of confidence in these projections, with little consistency found in the magnitude of the projected changes between either the models or the three analysis methods.
- Most simulations project an increase in the proportion of the most severe storms in the south-west Pacific and a southward movement in the latitude at which maximum intensity occurs.
- Most simulations project an increase in the proportion of storms occurring in the weaker categories in the Northern basin.
- Theory and high-resolution modelling also suggest that climate change may lead to a global increase in tropical cyclone intensity of about 2–11%.
- For the South Pacific, most models indicate a reduction in cyclonic wind hazard north of 20°S and regions of increased hazard south of 20°S. This coincides with the projected increase in the number of tropical cyclones occurring south of 20°S and with a poleward shift in the latitude at which storms are most intense.
- For the North Pacific region (between the equator and 15°N), there is a general reduction in cyclonic wind hazard between the current and future climate simulations as a result of a decrease in storm frequency close to the equator.

# 7.1 Introduction

This chapter deals with climate projections, including projections for extreme events such as tropical cyclones, based on dynamical and statistical downscaling. The methodologies are described in Chapter 4. Dynamically downscaled projections are presented for the CCAM 60 km simulations. This is followed by projections for Fiji and Papua New Guinea based upon two of the seven CCAM 8 km simulations. In Section 7.3, projections are presented for seven of the 17 sites that were statistically downscaled. Projected changes in tropical cyclones are presented using various techniques in Section 7.4. The results are summarised in Section 7.5.

- Downscaled PCCSP projections are generated using both dynamical and statistical downscaling.
- Dynamically downscaled atmospheric projections are provided at 60 km resolution using changes in sea-surface temperatures from six global climate models (Sections 4.1.2 and 4.3), driven by the A2 (high) emission scenario. Projections for two time periods centred on 2055 and 2090 are provided.
- Additional dynamically downscaled atmospheric projections are provided at 8 km resolution over seven PCCSP country regions each measuring 1000 x 1000 $km^2$ using CCAM, including changes in sea-surface temperatures from three global climate models, driven by the A2 high emissions scenario (Section 4.3). Projections are provided for two time periods centred on 2055 and 2090.
- Statistically downscaled projections for a total of 17 sites in seven Partner Countries for 2030 are provided. Projections out to 2055 are provided in some instances where observational data are of sufficient quality and length (approximately 40 years).
- Projected changes in tropical cyclones for the PCCSP region are obtained using several methods.
- Details of the methods underpinning the projections presented in this chapter were provided in Chapter 4.

# 7.2 Dynamical Downscaling

Dynamical downscaling is a methodology for providing more detailed climate projection information for a specific region. The technique uses broad-scale climate data from global climate models as input data for a finer resolution atmospheric model (see detailed discussion in Chapter 4). The main advantage of dynamical downscaling methods is that they rely on physically based modelling techniques similar to those used by the global models, but applied to regional scales (10–100 km). Dynamical downscaling is a process-based approach to how the rainfall, winds and temperatures change as global air temperatures increase. Dynamical methods can also be useful for studying extreme events (e.g. tropical cyclones).

## 7.2.1 CCAM Downscaling at 60 km Resolution

The first step in dynamical downscaling in this study was to run CCAM with a global grid of 60 km resolution using bias-adjusted sea-surface temperatures from six global climate models for the period 1961–2099. Projections based upon these simulations are presented here and compared with those from the host global models.

### 7.2.1.1 Surface Air Temperature

The projected changes in near-surface maximum and minimum air temperature (Figure 7.1) are similar to those from the host global models since the changes in the sea-surface temperatures in the simulations using CCAM are the same as those for the global models. In general, the warming across the region is 2–3°C by the end of the 21st century for the A2 (high) emissions scenario, although some regions warm by more than 3°C. Although not shown, the simulation using sea-surface temperatures from the UKMO-HadCM3 model warms the least (around 2.5°C). The simulation using sea-surface temperatures from CSIRO-Mk3.5 warms the most (closer to 3.5°C). The mean maximum temperature change based on the average of all six models shows generally greater warming along the equator in the central and eastern Pacific, as well as over Australia and surrounding oceans, whilst the least warming occurs over the south-eastern

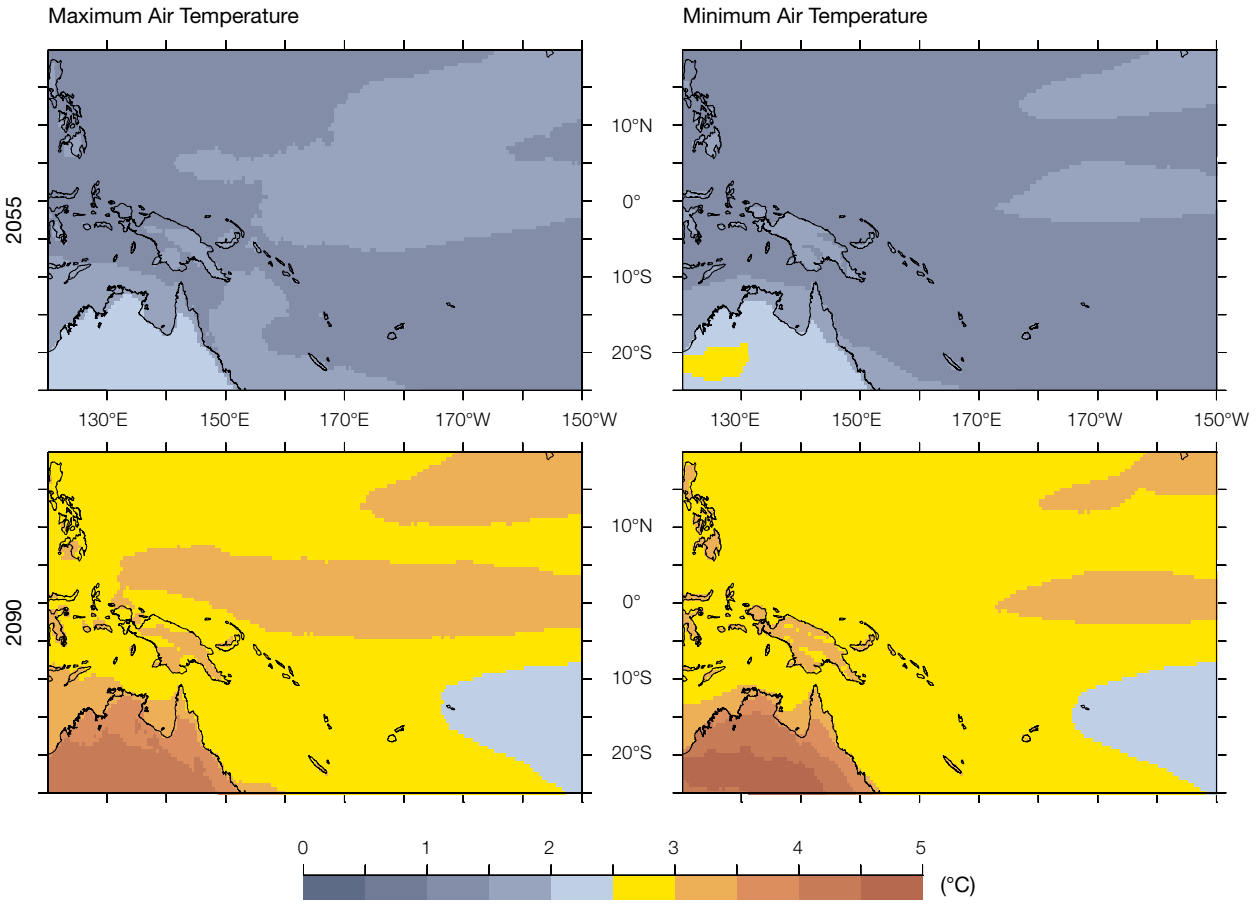


**Figure 7.1:** Increases in annual maximum near-surface air temperature (°C) (left) and minimum temperature (right) in 2055 (top) and 2090 (bottom) relative to 1990 for the CCAM 60 km multi-model simulations using the A2 (high) emissions scenario.

Pacific. Minimum temperature changes show a similar spatial pattern (see Figure 6.2 for comparison with mean surface-temperature changes in the global models). Also note the increased warming over the better resolved land areas in the downscaled results.

### 7.2.1.2 Rainfall

Simulations driven by the six host sea-surface temperatures downscaling to 60 km with CCAM (Figure 7.2 for November-April and Figure 7.3 for May-October) show that the broad-scale changes in rainfall are generally similar to those of the host models, with increases along the equator and smaller changes elsewhere. These results suggest a significant influence of the sea-surface temperature changes on the rainfall changes. There is an increase in rainfall of approximately 2–3 mm per day along the equator, with a decrease in rainfall of up to 2 mm per day for latitudes around 8° north and south of the equator. The location and intensity of these changes are different in the host models and the downscaling model. In general, the largest increases in rainfall in the CCAM simulations are closer to the equator, while the greatest increases in the global models tend to be located at about latitude 5°S, especially in the central and eastern portions of the domain. These differences could be related to the downscaling method chosen, which corrects some of the sea-surface temperatures biases in the global models (see discussions in Chapter 4 and Chapter 5).
The decreases in rainfall in the downscaled simulations north and south of the equatorial region also tend to be somewhat larger and cover a much broader area than in the global models, particularly in the period November-April. A possible explanation for the rainfall differences in CCAM and the global models relates to changes in the Hadley Circulation, since with enhanced convection along the equator, there is greater ascent of air. Compensating subsidence to the north and south will tend to suppress the rainfall. In the finer-resolution CCAM simulations, this compensating subsidence appears to be stronger than in the global models. As will be shown later, some of the additional downscaled simulations also show similar rainfall decreases on either side of the equatorial region, which suggest this is related to resolution. This is an area for further research.

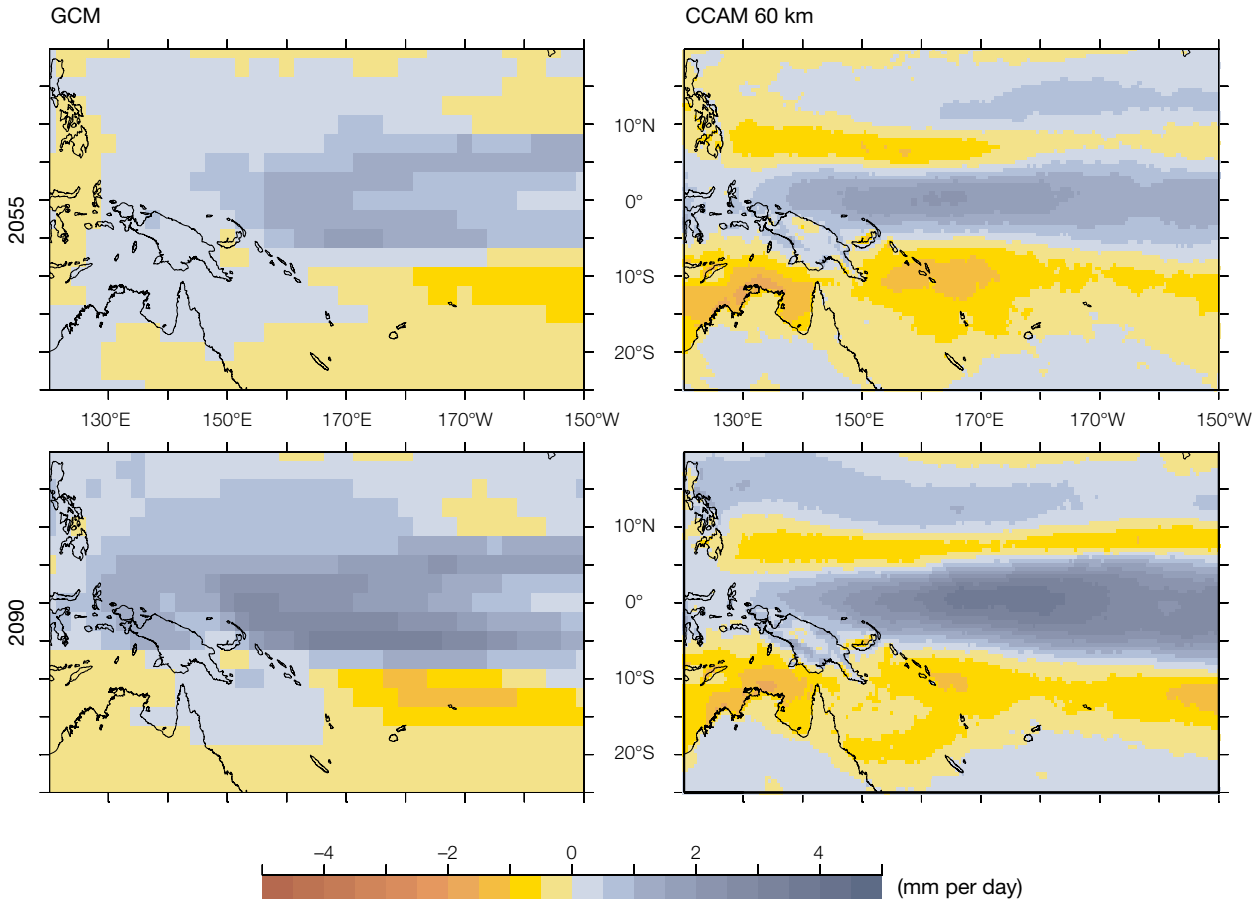


Figure 7.2: Multi-model mean change in November-April rainfall (mm per day) in global climate models (left) and CCAM 60 km simulations (right), each consisting of the same six models, for the period centred on 2055 (top) and 2090 (bottom), relative to 1990, using the A2 (high) emissions scenario.

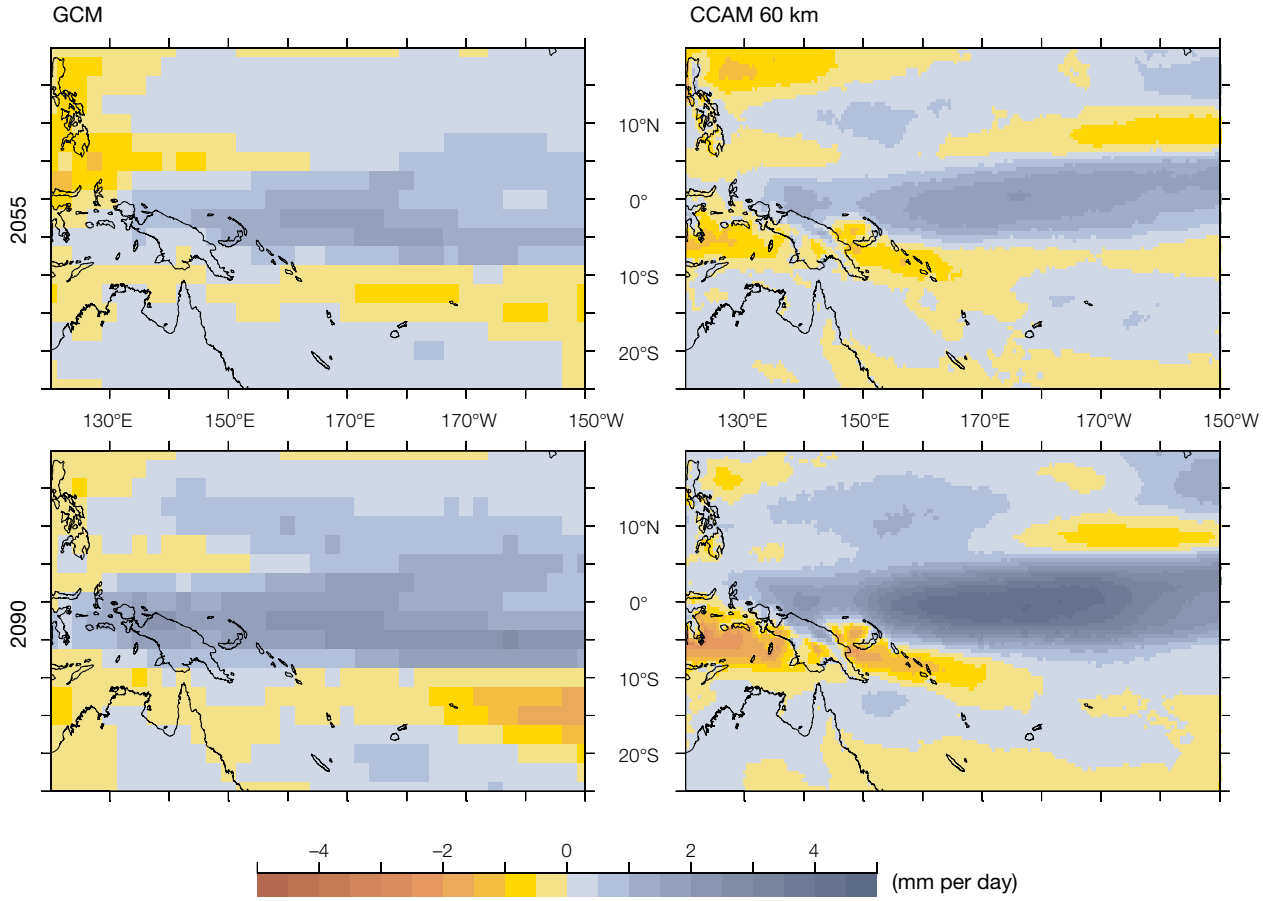


**Figure 7.3:** Multi-model mean change in May-October rainfall (mm per day) in global climate models (left) and CCAM 60 km simulations (right), each consisting of the six models, for the periods centred on 2055 (top) and 2090 (bottom), relative to 1990, using the A2 (high) emissions scenario.

In order to check the consistency of these rainfall changes among the six downscaled simulations, the annual rainfall changes from 2055 and 2090 were compared (Figure 7.4). As indicated earlier, results show that the largest increases are along the equator, with greater increases by 2090. Bands of rainfall decreases around latitudes 8°N and 8°S are also evident. The six CCAM simulations all agree on the equatorial increase in rainfall due to the greater warming of the sea-surface temperatures along the equator. Most simulations (five out of six) also show a decrease in rainfall in bands to the north and south of this increase. While the global models show a similar equatorial increase, they tend not to show the decreases to the north and south (Chapter 6).

The changes in rainfall along the South Pacific Convergence Zone (SPCZ) are small, though there is some agreement in decreases around Vanuatu and over the south central Pacific. Rainfall decreases are evident over the oceans north of Australia and East Timor, and are very consistent across all the downscaled results.

### 7.2.1.3 Surface Wind Speed

CCAM simulations of the projected change in wind speed (at 10 m above the surface) over the PCCSP region (Figure 7.5) do not indicate a major change in wind speed by the end of the 21st century, with a projected reduction in wind speed of less than 1 metre per second on average. The magnitude of wind speed decreases is 0.5 metre per second in south-western regions. The MIROC3.2 (medres)-based CCAM simulation shows the greatest increases, but this model is considered unreliable in the SPCZ and West Pacific Monsoon regions. The general pattern of wind speed change is similar to the global climate models (Figure 6.5), although increases south of the equator are slightly less than for the global models.

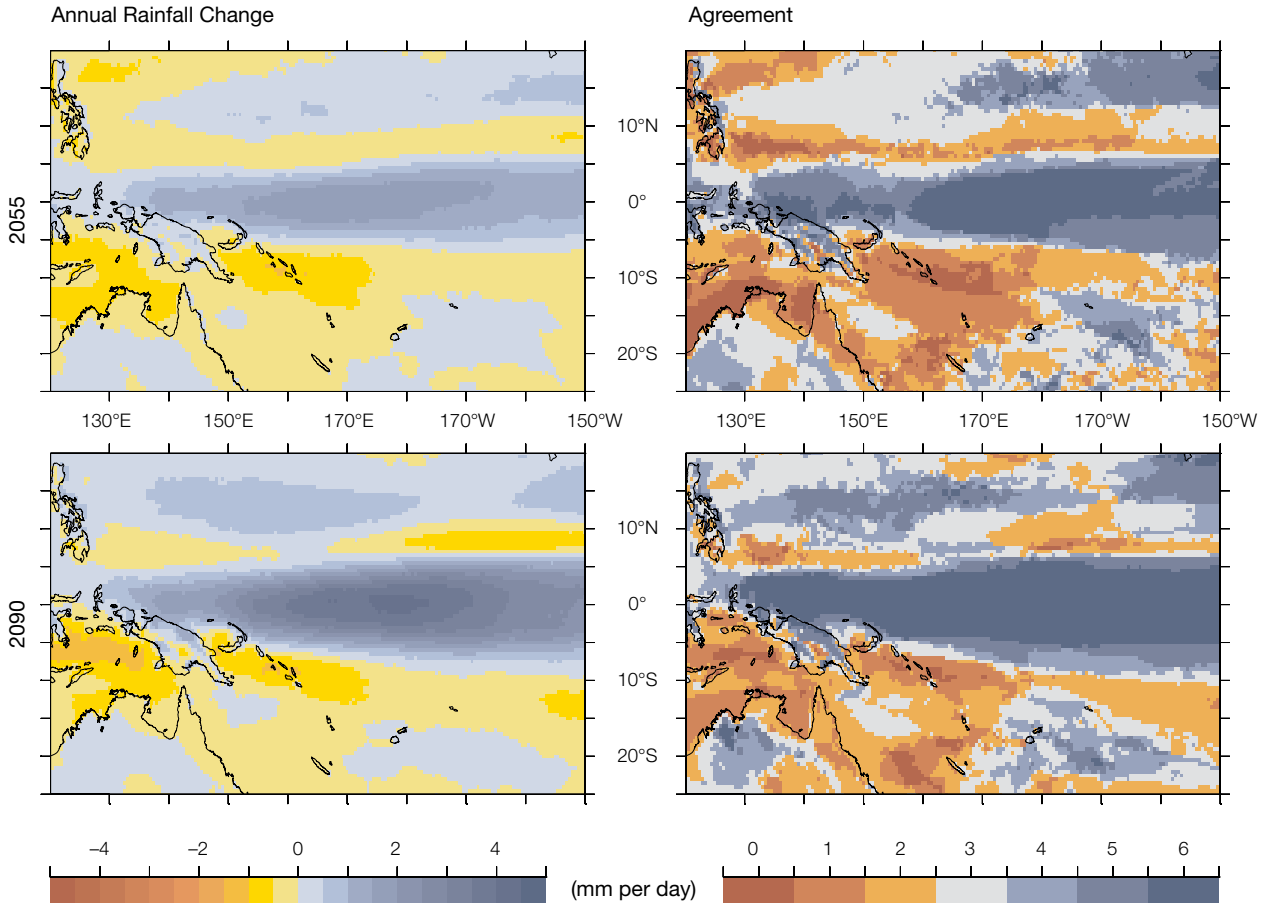


Figure 7.4: Annual change in rainfall (mm per day) between the periods centred on 2055 (top left) and 2090 (bottom left) relative to 1990, and the agreement on an increase in the six CCAM simulations for the same two periods (right top and bottom). 0 means all models show a decrease, 6 means all show an increase.

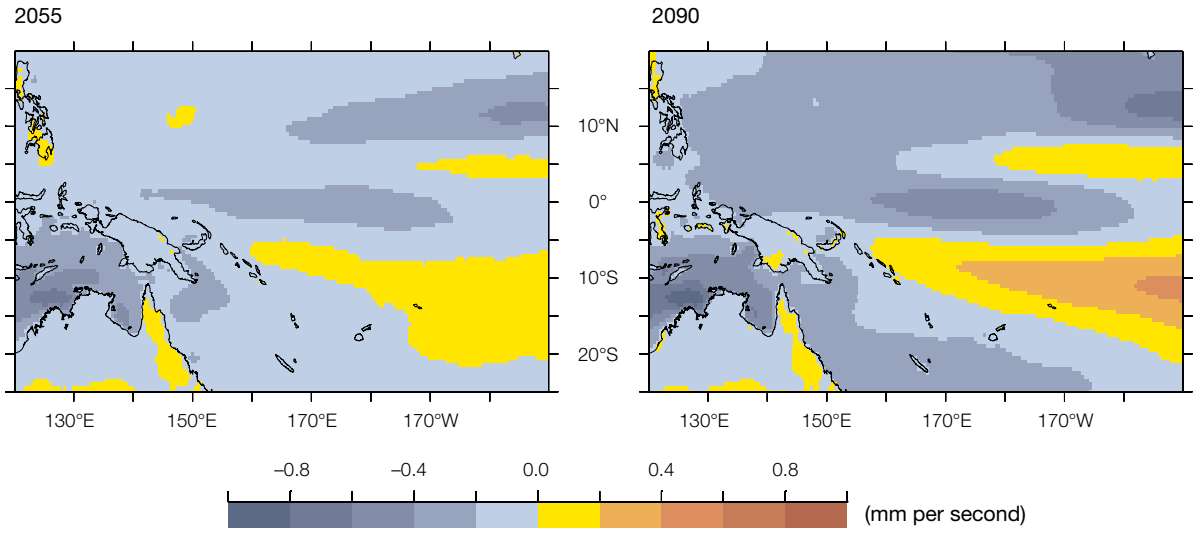


Figure 7.5: Mean change in annual 10 m wind speed (metres per second) between the periods centred on 2055 (left) and 2090 (right) relative to 1990 (from the multi-model mean of the six CCAM 60 km simulations, for the A2 (high) emissions scenario).

### 7.2.1.4 Heavy Rainfall

Projected changes in number of days per year with heavy rainfall (that is, days with daily rainfall between 20 and 50 mm) by 2090 are given in Figure 7.6. There are increases along the equator in the multi-model means of all of the global climate models, as well as for the five global models with daily data that were downscaled and the six CCAM 60 km simulations. The mean of all global climate models shows increases of 5-10 days per year, while the 5-global model mean has increases of up to 20 days per year near Vanuatu and Papua New Guinea. The pattern of change is similar for the two sets of global model simulations, with one band of increase south of the equator near 5°S and another band near 5°N. The CCAM 60 km simulations show much larger increases in number of heavy rainfall days (more than 35 days per year in some areas), and the locations are more centred on the equator. In addition, there are decreases (more than 10 days per year) near Vanuatu and north of Australia.

## 7.2.2 CCAM Projections Downscaled to 8 km Resolution

Three of the CCAM 60 km simulations (driven by sea-surface temperatures from host global climate models ECHAM5, HADCM3, and GFDL2.1) for the A2 (high) emissions scenario were further downscaled to 8 km resolution over seven regions, each measuring approximately 1000 x 1000 km$^2$. This was conducted to assess the impact of the finer resolution downscaled results on the projected changes. Two 20-year time periods were completed, centred respectively on 2055 and 2090, and compared to the 20-year period centred on 1990. The seven regions selected were Papua New Guinea, East Timor, Fiji, Solomon Islands, Vanuatu, Samoa and the Federated States of Micronesia. In the next section, summary results for two regions are examined; more detailed assessment and results for the other regions will be presented in a future technical report.

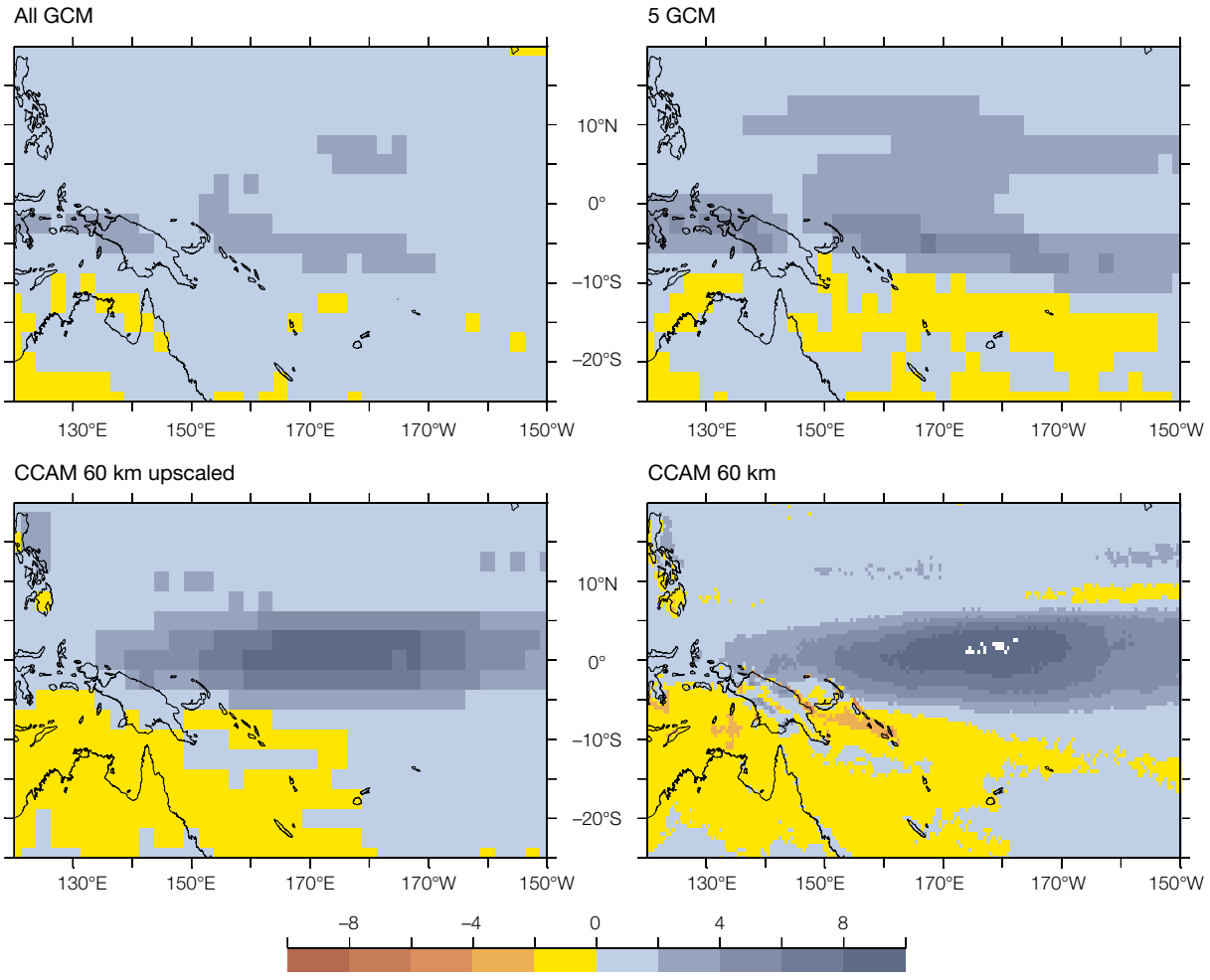


**Figure 7.6:** Change in number of heavy rain days between 2090 and 1990 using multi-model means of all global climate models (top left), five global models used for downscaling with daily data (top right) and CCAM 60 km simulations. Upscaled (bottom left) and on original grid (bottom right).

### 7.2.2.1 Detailed Analysis of Two Regions at 8 km Resolution

In this section, two regions are analysed in order to explore any improvement in the detail of local projections, particularly over mountainous areas (Section 4.5.2). Papua New Guinea was chosen since this region has the most varied and mountainous topography. Fiji was also selected since it has some mountainous topography and is of moderate size for a Pacific Island nation. In addition, two stations on Fiji with observational data available are further analysed. The following results need to be treated with caution because they are based on a very limited sample of global climate models and only one dynamical downscaling model.

Over Fiji, the downscaled 8 km simulations show maximum temperature increases of 2–2.5°C over the ocean (Figure 7.7), with greater warming over the land (up to 3–3.5°C over the western side of Viti Levu, the south-west island) in May-October. In November-April, the maximum temperature increase is 2.5–3°C. Minimum temperatures increase similarly (2–2.5°C in May-October and 2.5–3°C in November-April), with around 0.5°C greater warming evident over the land.

The projected rainfall changes show increases of 0.5–1 mm per day in May-October (Figure 7.7), with greater increases (up to 1.5 mm per day) along the eastern side of the islands. Rainfall decreases of 0.5–1 mm per day are evident in November-April, especially along the southern and eastern side of the islands. In addition, there is some increase in rainfall over the north-west side of Viti Levu.

Over Papua New Guinea during May-October, the maximum temperature increase is around 2.5°C over the ocean (Figure 7.8) and 3–4°C over the land. In November-April, the ocean warms 2.5°C while the land warms 3.5–4°C. Minimum temperatures increase around 2.5°C over the oceans and around 3°C over land in May-October and 2.5–3°C over the oceans and 3–3.5°C over land in November-April.

The projected rainfall changes for Papua New Guinea (Figure 7.8) show a complicated pattern related to the topography. There are rainfall increases over the ocean to the north and south of Papua New Guinea, and some decreases between Papua New Guinea and New Britain. Over land, the projected rainfall increases are along the northern slopes of the mountain ranges, with some decreases on the southern sides. There are general projected decreases of rainfall across the region in May-October, apart from some increases along the mountain ranges.

These results demonstrate the added information that dynamical downscaling provides. The high resolution (8 km) simulations can capture some of the effects of the topography and land-sea contrast on the climate projections. As seen in the temperature projections, the greater warming over land versus the oceans is captured. Spatial variations in the projected rainfall changes are also evident. (For further discussion of how downscaling can add value to coarser resolution models, see Corney et al., 2010; Frauke et. al., 2011; Kanamitsu and DeHann, 2011; Rockel et. al., 2008.)

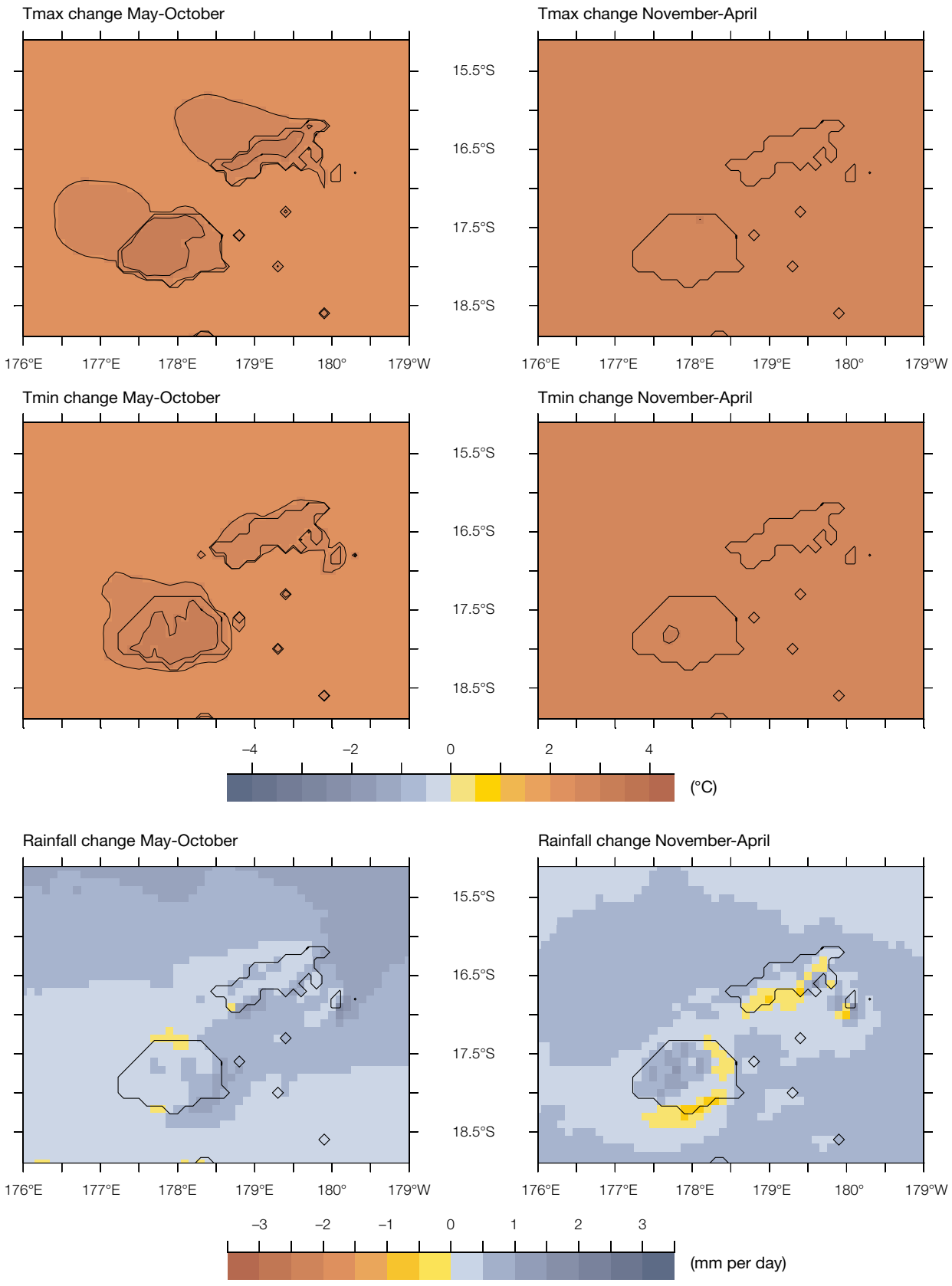


**Figure 7.7:** Projected temperature and rainfall changes for Fiji in 2090 relative to 1990 from CCAM 8 km multi-model mean simulations, for the A2 (high) emissions scenario. Left panels are May-October and right panels are November-April. Top row is changes in maximum surface air temperature (°C), middle row is changes in minimum surface air temperature (°C) and bottom row is changes in mean rainfall (mm per day).

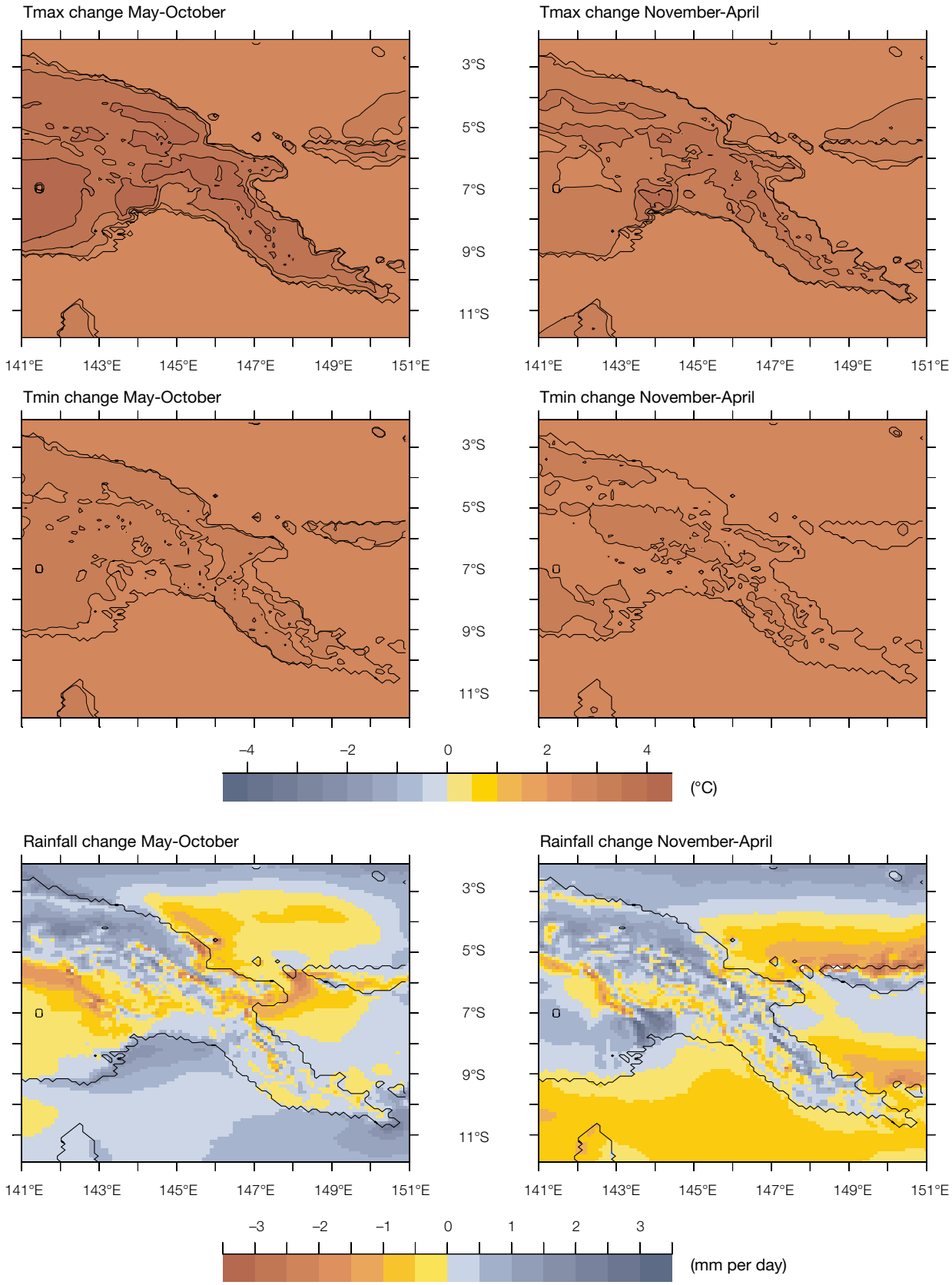


**Figure 7.8:** Projected changes in temperature and rainfall for Papua New Guinea in 2090 relative to 1990 from CCAM 8 km multi-model mean simulations, for the A2 (high) emissions scenario. Left panels are May-October and right panels are November-April. Top row is changes in maximum surface air temperature (°C), middle row is changes in minimum surface air temperature (°C) and bottom row is changes in rainfall (mm per day).

### 7.2.2.2 Seasonal Temperature and Rainfall Changes at Selected Locations

Changes in seasonal rainfall and temperature can also be significant. The comparison of changes in temperature and rainfall for Nadi, Fiji for the global climate models, CCAM 60 km simulations, and CCAM 8 km simulations are presented in Figure 7.9. As was indicated in Figure 7.7, which covers all of Fiji, the temperature increases about 1.5°C by 2055 and by 2.5–3°C by 2090. There are slightly greater temperature increases in the middle of the year, most noticeably in the 8 km simulations, where increases are around 3.5°C.

There are only slight rainfall changes by 2055 in the global climate models and the CCAM 60 km results. The 8 km simulations show small increases at Nadi throughout most of the year. By the end of the century, all simulations show rainfall increases in the first half of the year, with greater increases in the 8 km simulations than in the 60 km simulations. The second half of the year shows little change in rainfall (Figure 7.9, lower right).

The seasonal changes in temperature and rainfall for Nausori, Fiji are presented in Figure 7.10. As was indicated in Figure 7.7, the temperature warms about 1.5°C by 2055 and by 2.5–3°C by 2090. There is slightly greater warming in the first half of the year (nearing 3°C) while warming is only 2.5°C later in the year. Note that the changes for the global models are similar for Nadi and Nausori, since they are separated by just over 100 km, less than the grid spacing of the models.

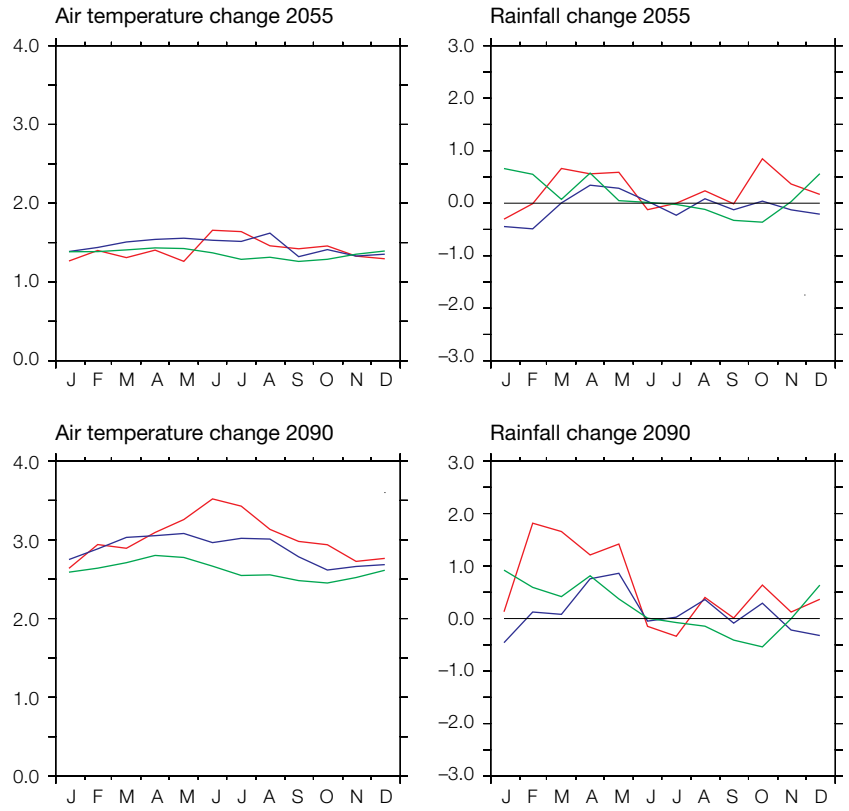


**Figure 7.9:** Monthly changes in surface air temperature (left, ˚C) and rainfall (right, mm per day) for Nadi, Fiji, showing changes in 2055 (top) and 2090 (bottom) relative to 1990, for the A2 (high) emissions scenario. Green lines are changes for global climate models, blue are changes for CCAM 60 km, red are changes for CCAM 8 km simulations.

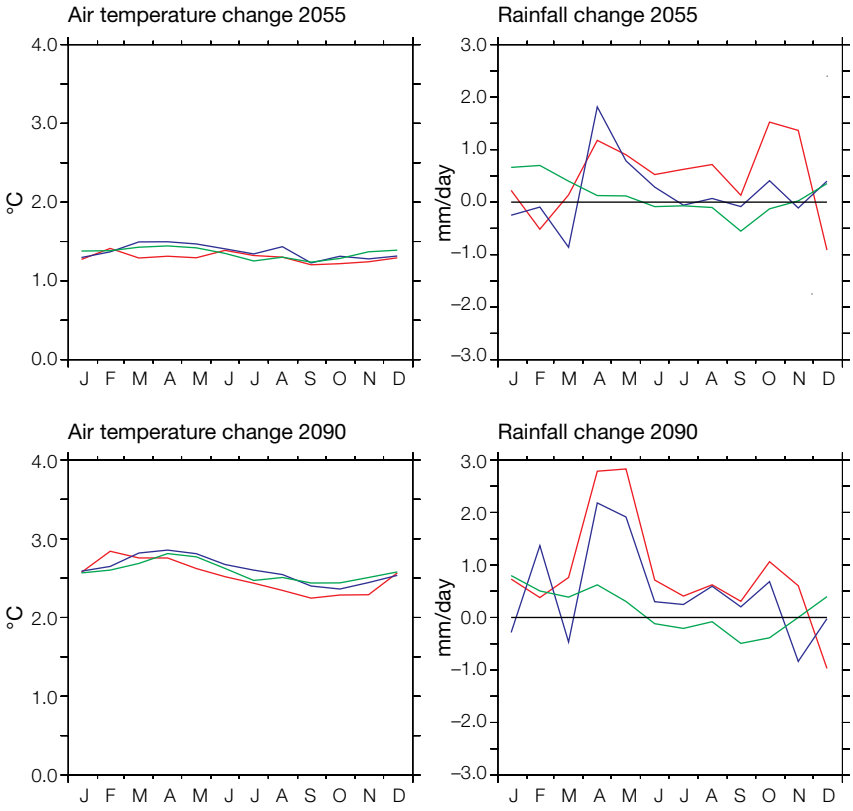


**Figure 7.10:** Monthly changes in temperature (left, ˚C) and rainfall (right, mm per day) for Nausori, Fiji, showing changes in 2055 (top) and 2090 (bottom) relative to 1990, for the A2 (high) emissions scenario. Green lines are changes for global climate models, blue are changes for CCAM 60 km, red are changes for CCAM 8 km.

Rainfall generally increases throughout the year for Nausori, though the changes in the global models are very small (and show some decreases in second half of the year). In the CCAM 60 km and 8 km downscaled projections, the rainfall increases are greatest in April and May.

### 7.2.2.3 Changes in Probability Density Functions of Temperature and Rainfall at Selected Locations

In order to assess the changes in the frequency of various daily rainfall amounts and to compare the various projected changes, the frequency distribution or probability density functions (PDF) of temperature and rainfall changes for two locations in Fiji are analysed. Fiji was selected since it is a relatively small, mountainous island, not resolved by the global climate models, has only one grid point at 60 km, and is reasonably well resolved at 8 km grid spacing. It is expected that the benefits of downscaling will be more evident at finer resolution. It should be noted that looking at only selected locations can be misleading as an indication of broader changes, since as was shown previously, there can be significant gradients of change over small distances related to local effects such as topography.

Changes in the PDFs of temperature and rainfall for Nadi are shown in Figure 7.11. As expected with global warming, there is a decrease in frequency of cooler temperatures and an increase in frequency of warmer temperatures. There is a slightly greater shift to warmer temperatures in the 8 km results because of the greater warming of the better-resolved land mass.

The projected changes in the rainfall PDF are generally small, with changes of only 1–2% in frequency. By 2055, the global climate models show little change in the frequency of rainfall, although there are slight decreases in light rainfall and slight increases in heavy rainfall. The CCAM 60 km and 8 km results show decreases in frequency of no rain days. The 60 km results show about 1% increase in frequency of the 4–10 mm per day rain days and decreases in frequencies for rain days greater than 10 mm per day. The 8 km results show increases in frequency of the 6–16 mm per day rain days. By 2090, the changes in frequency are generally similar to those for 2055.

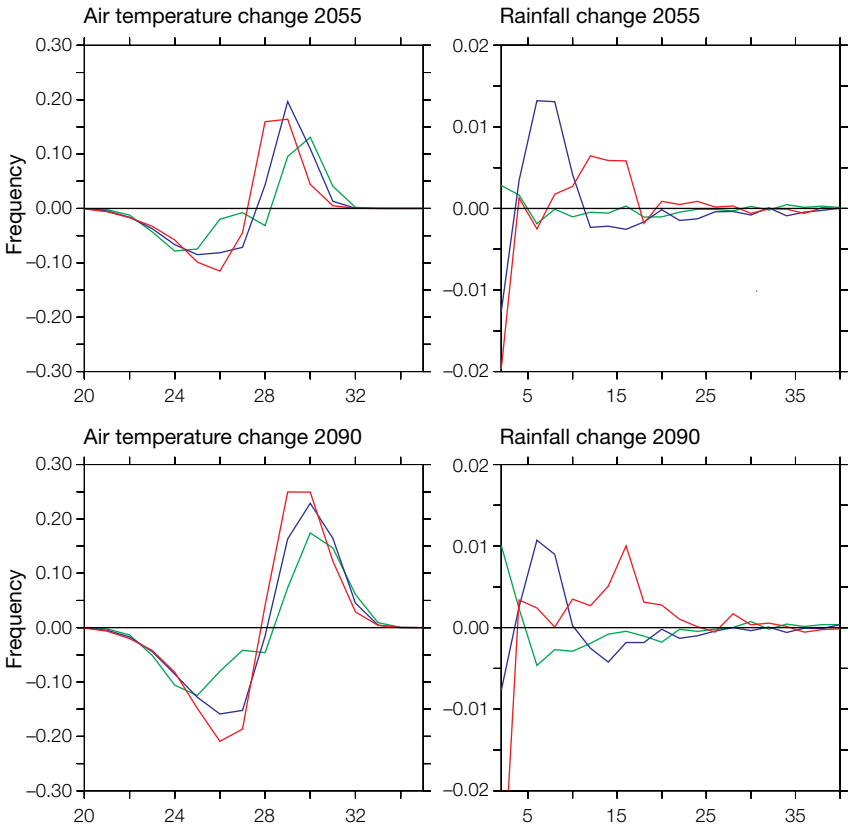


**Figure 7.11:** Changes in probability density functions for temperature (left, °C) and rainfall (right, mm per day) for Nadi, Fiji. Top row shows changes in 2055 relative to 1990, and bottom shows changes in 2090 relative to 1990, for the A2 (high) emissions scenario. Green lines are changes for global climate models, blue are changes for CCAM 60 km, red are changes for CCAM 8 km.

Changes in the PDFs of temperature and rainfall for Nausori are shown in Figure 7.12. There is a decrease in frequency of cooler temperatures and an increase in frequency of warmer temperatures, as for Nadi. The changes in the 8 km results show less of an increase than the 60 km simulations. The likely cause of this is related to the ocean influence on land. For the 60 km grid, a land point is 60 km away from the ocean, so coastal land points will have only minimal oceanic influence. For the 8 km grid, coastal land points are closer to ocean grid points, and hence the ocean will have a much greater influence, especially when there is onshore flow. For Nausori on the upwind side of Fiji, the effect of the weaker warming of the ocean relative to the land will be greater in the 8 km grid than in the 60 km grid. In the global models, Fiji is an ocean point. As a result, for Nausori, the 8 km projected temperature changes are closer to the global models than the 60 km results. Note this is not the case for Nadi, since Nadi is on the leeward side of the island and will be less influenced by the ocean.

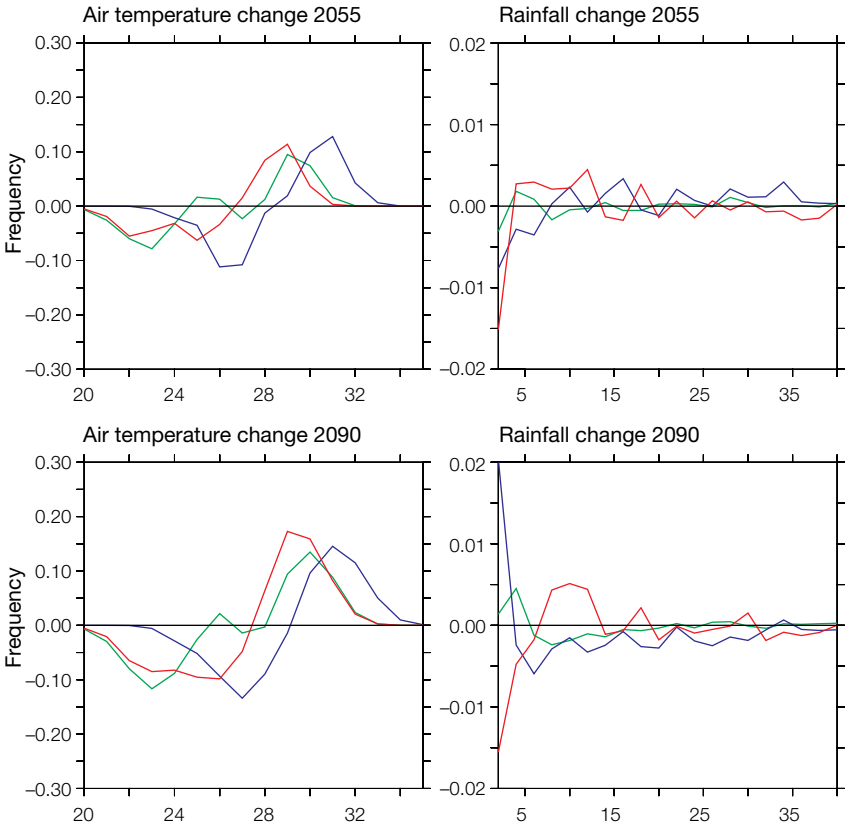


**Figure 7.12:** Changes in probability density functions for temperature (left, °C) and rainfall (right, mm per day) for Nausori, Fiji. Top row shows changes in 2055 relative to 1990; bottom shows changes in 2090 relative to 1990, for the A2 (high) emissions scenario. Green lines are changes for global climate models, blue are changes for CCAM 60 km, red are changes for CCAM 8 km.

The changes in rainfall PDF are very small by 2055, though all models tend to show a decrease in no or light rain days. By 2090, the global climate model changes are still small, but the 60 km projections show increases in no rain days, and decreases in other rainfall days. However, the 8 km results show a continued decrease in the frequency of no rain days, and an increase in frequency of moderate rain days with 8–12 mm per day.

### 7.2.2.4 Extremes

Changes in the frequency of the 1-in-20-year daily maximum air temperature for Fiji at 2055 and 2090 are shown in Figure 7.13. Increases in extreme maximum temperatures are mostly less than 2°C by 2055, but they increase to over 4°C by 2090 over land. Over the ocean, changes are around 3°C. For rainfall, the projected change in the number of heavy rainfall days (annual frequency of daily rainfall between 20 mm and 50 mm) are presented in Figure 7.14 for 20-year periods centred at 2055 and 2090. By 2055, the number of heavy rainfall days increases only slightly to the east and north of Fiji, and decreases slightly to the south-west. By 2090, the increases to the north of Fiji are greater than five days per year, while there are some decreases along the eastern side of Viti Levu. There are also some increases of over five days over central parts of the island. Note that Fiji lies in a region of small changes in the global climate models and CCAM 60 km simulations (Figure 7.6).

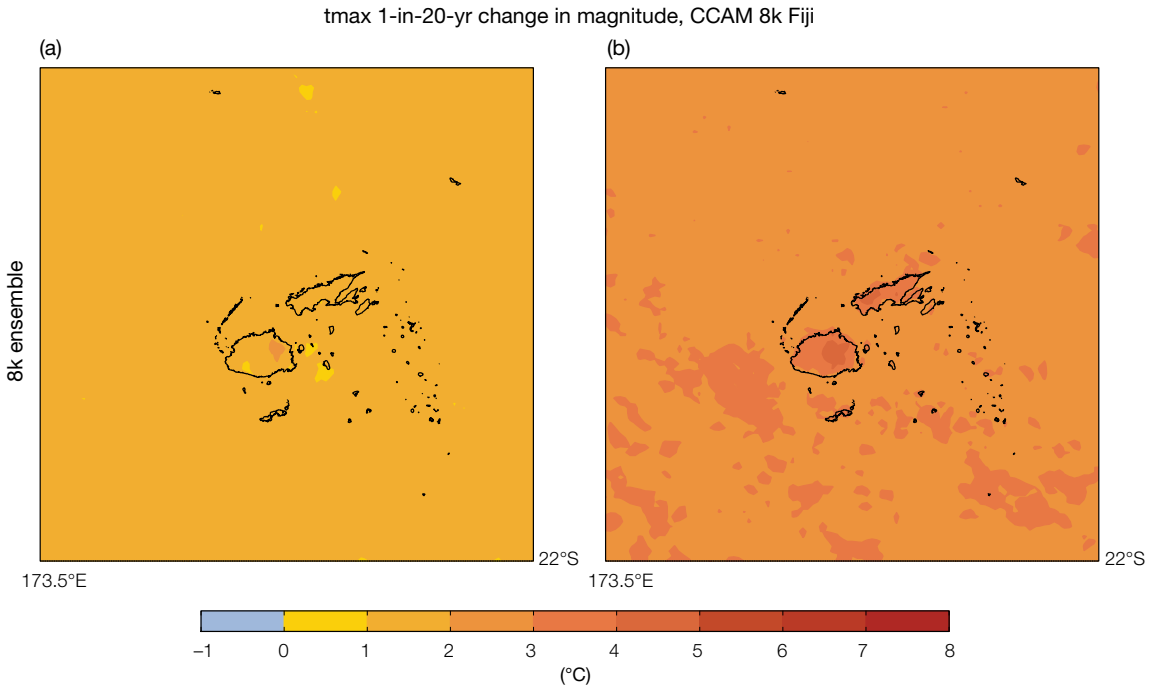


**Figure 7.13:** Change in magnitude of 1-in-20-year daily maximum air temperature events (°C) for Fiji, showing changes between the periods (a) 2055 and (b) 2090 relative to 1990, for the CCAM 8 km multi-model mean with the A2 (high) emissions scenario.

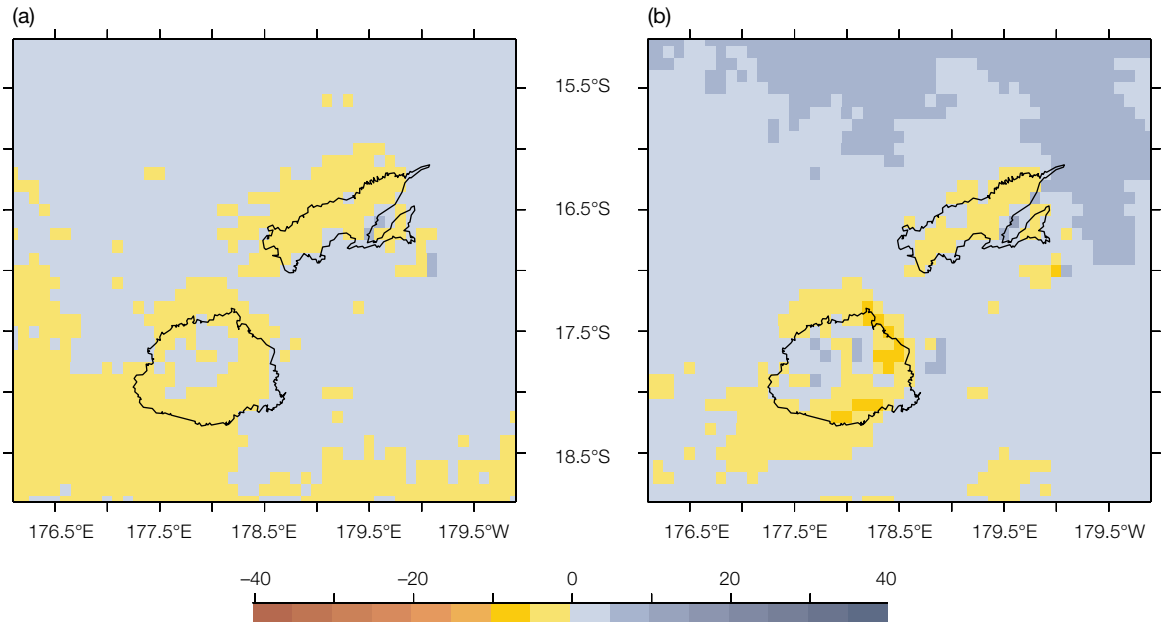


**Figure 7.14:** Change in the number of days with heavy daily rainfall for Fiji, showing changes between the periods 2055 (a) and 2090 (b) relative to 1990, for the CCAM 8 km multi-model mean with the A2 (high) emissions scenario.

Changes in the 1-in-20-year daily maximum air temperature for Papua New Guinea are shown in Figure 7.15. Increases in extreme maximum temperatures are projected to be mostly less than 2°C by 2055, except for the higher mountains where changes of over 2°C are evident. However, by 2090, the extreme daily temperatures increase over the mountains by more than 5°C. Over the ocean, increases are around 2.5°C. The number of heavy rain days per year (Figure 7.16) increases by more than five days to the north of Papua New Guinea, as well as over some mountainous regions and over the Gulf of Papua by 2055. There are also decreases of more than five days in heavy rain days along the north of New Britain, the Solomon and Coral Seas and in a band extending inland from the Gulf of Papua. By 2090, the general pattern is similar, but the changes are slightly larger.

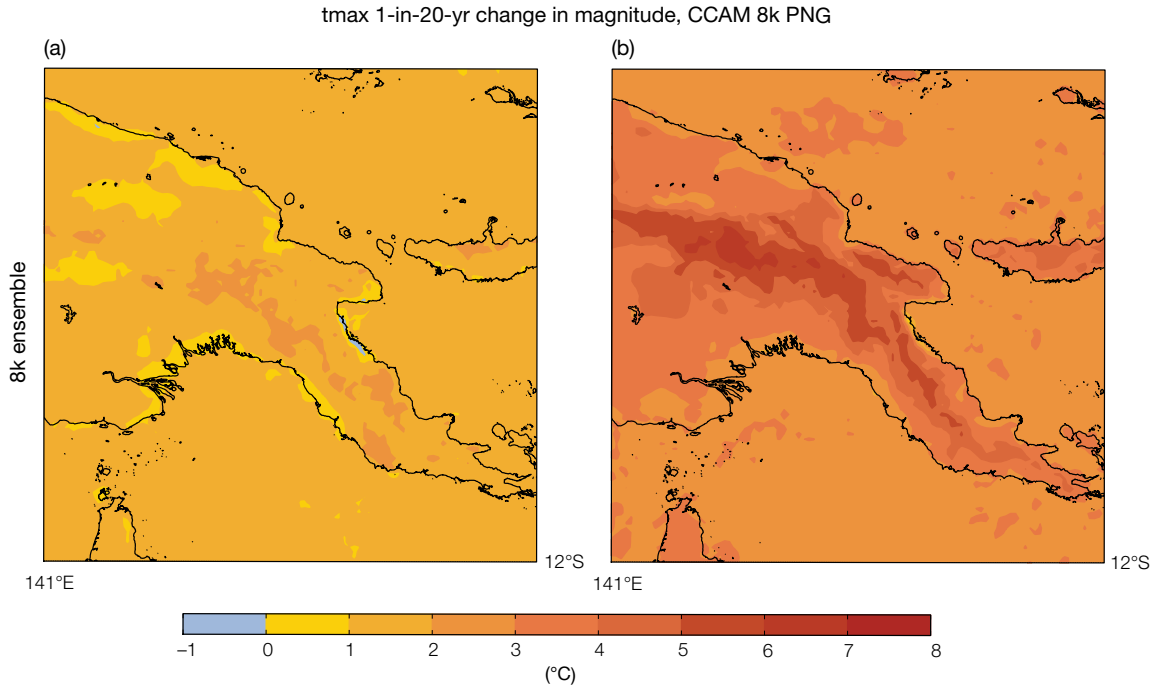


**Figure 7.15:** Change in magnitude of 1-in-20-year daily maximum air temperature (°C) events, showing projected changes for Papua New Guinea between the periods (a) 2055 and (b) 2090 relative to 1990, for the CCAM 8 km multi-model mean with the A2 (high) emissions scenario.

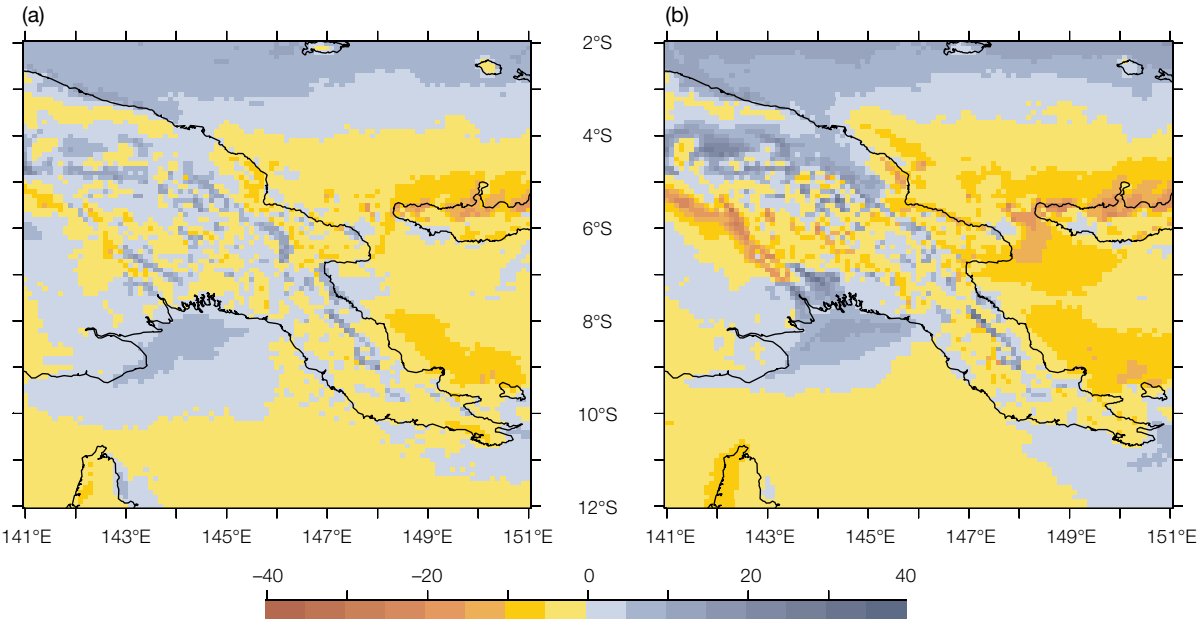


**Figure 7.16:** Change in the projected number of days with heavy daily rainfall for Papua New Guinea, showing changes between the periods (a) 2055 and (b) 2090 relative to 1990, for the CCAM 8 km multi-model mean with the A2 (high) emissions scenario.

## 7.2.3 Additional Regional Climate Model Results

Rainfall projections from the additional downscaling simulations are presented in Figure 7.17. The host global climate model is GFDL2.1, which was downscaled to 60 km with CCAM before providing data to the additional downscaled simulations. All simulations except the MM5 simulation, which was excluded due to its poor representation of the current climate (Section 5.3.3), show increases in rainfall along the equator of 1 to 3 mm per day. To the north and south of this increase, there tend to be bands of decrease, similar to the CCAM 60 km results. These bands of decreased rainfall are not as evident in the global models (Figure 6.4). There is less consistency in the results in the western portion of the domain. It is possible that the increased rainfall along the equator gives rise to greater upward motion, with compensating subsidence to the north and south causing an associated decrease in rainfall. These results may also be a result of the finer resolution, but the processes causing these changes need further investigation.

These results are some of the first multi-model dynamically downscaled simulations for the equatorial Pacific. Although there are some differences in the projected rainfall changes between the models, the differences are much less than among the various global models. This is possibly due to all models having the same bias-corrected sea-surface temperatures. In addition, all models used the same CCAM 60 km atmospheric conditions as lateral boundary conditions. However, the downscaled simulations all used different model dynamics, physics and model set-ups.

## 7.2.4 Dynamical Downscaling Summary

Dynamical downscaling at 50 to 60 km resolution indicates increased rainfall near the equator, between about 10°N and 10°S. Projected drying outside this band is likely as a result of the more intense rainfall along the equator. The models used in this study have very different dynamics, physics and set-up. The fact that they produce similar results adds confidence to the projections. In addition, the 8 km dynamical downscaling results are able to capture the significant effects of the mountainous topography on projected changes in temperature and rainfall across islands, as well as the seasonal variations of rainfall rate and location, and the greater warming of the islands than the surrounding oceans. Although it must be remembered that high-resolution dynamically downscaled models do not provide conclusive evidence of future climate, they are able to suggest trends that cannot be captured by models with coarser grids, where the islands are not resolved.

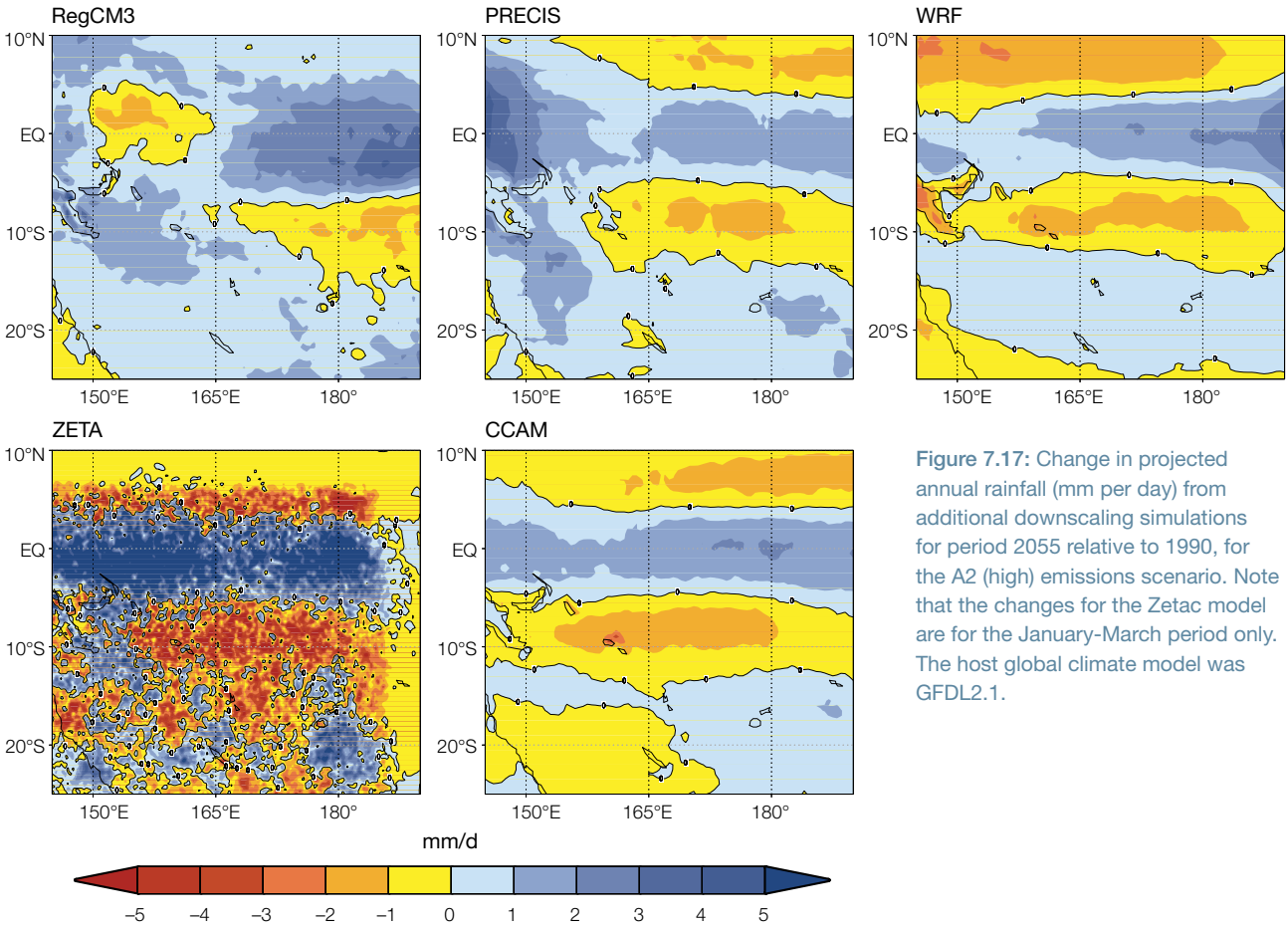


**Figure 7.17:** Change in projected annual rainfall (mm per day) from additional downscaling simulations for period 2055 relative to 1990, for the A2 (high) emissions scenario. Note that the changes for the Zetac model are for the January-March period only. The host global climate model was GFDL2.1.

# 7.3 Statistical Downscaling

Despite the significant improvement in spatial detail achieved via dynamic downscaling, this approach still has some limitations regarding accurately resolving all physical and synoptic-scale features, as well as predicting trends in climate at specific locations (Section 7.2). This is where statistical downscaling may play an important bridging role by empirical modelling of the relationship between carefully selected covariates from CCAM 60 km simulations and observed climate at specific locations over the observation period. The statistical approach selects the best set of covariates for each location which include the variable being downscaled, e.g. rainfall or temperature, as well as others such as sea-level pressure, total cloud and water mixing ratio.

The relationships between these covariates and the station observations are then used by the statistical model to make projections. Future changes in the CCAM covariates are used to produce station-scale future projections. This implies that the observed trends of climate at a specific location will influence the future projected value at that location. For this reason only locations with high quality data and long observational histories were chosen for downscaling.

## 7.3.1 Statistical Downscaling Results

The results of statistical downscaling (Table 7.1) based on output from three of the CCAM 60 km simulations (Section 4.6) show a projected increase in average daily rainfall in most locations for most host models, except for the Marshall Islands, where average daily rainfall is projected to decline in two out of the three cases. In some locations, the range of rainfall projections is quite wide, e.g. in the Federated States of Micronesia and the Marshall Islands, which indicates that rainfall is projected with less certainty in these locations. Average maximum and minimum temperature are consistently projected to increase in all locations regardless of which CCAM simulation is used to drive the statistical downscaling.

A comparison of median historical changes in temperature and rainfall between station observations and CCAM downscaled simulation data (not shown) revealed that results from the ECHAM5/MPI-OM model were most closely aligned with station changes across the Pacific. For this reason, the discussion and tables that follow focus on results from the ECHAM5/MPI-OM model. In most locations and seasons, rainfall is projected to increase (Table 7.2). A decline in daily rainfall across all seasons is projected in the Marshall Islands and a somewhat smaller decline across all seasons is projected for Samoa. In the case of the Marshall Islands, this is due to reductions in the intensity of rain, coupled with the increase in rain days, whereas for Samoa no decline in rain days is projected. The findings for these two locations are supported by the observed trends in the climate data at these locations. For example, for Majuro, Marshall Islands, the trend in median rainfall on rain days is -0.12 ± 0.02 mm per year, and the trend in rain days is +0.4 ± 0.06 % per year over the time period that data have been observed. Given the length of this observation time period (1973–2009) we can be quite confident that these trend estimates are not overly influenced by short-term effects.

For Nadi, Fiji, the number of rain days is projected to have little change by 2021–2040 (Table 7.2). However the median and 90th percentiles of rainfall are projected to increase, suggesting that events may decline in frequency but increase in severity. Again, this result is supported by trends in the observed data: the median rainfall on rain days increases at the rate of 0.08 ± 0.02 mm per year and the number of rain days decreases by 0.3 ± 0.1% per year over the observation period (1961–2009).

A comparison of the average change in rainfall projected by the dynamically downscaled ECHAM5/MPI-OM model compared to the statistical downscaled projections shows some differences (Table 7.2). These differences may be due to statistically significant differences in the trend of observed climate data and dynamically downscaled ECHAM5/MPI-OM data at the specific locations (highlighted by * in Table 7.2). For example, at Lamap in Vanuatu the trend in observed rainfall is 0.06 mm per year whereas for the dynamically downscaled ECHAM5/MPI-OM data over the same time period it is a very small decline. The statistical model not only uses dynamically downscaled ECHAM5/MPI-OM rainfall to project the future changes, but other variables such as sea-level pressure, temperature, and total cloud as well.

**Table 7.1:** Change in statistically downscaled climatic statistics projected for seven locations in the Pacific between 1981–2000 and 2021–2040. The statistical downscaling projections are based on output from three CCAM simulations (Section 4.6) under the A2 (high) emissions scenario. Values are sorted in ascending order.

| Location | Change in average rainfall (mm per day) | | | Change in median maximum temperature (°C) | | | Change in median minimum temperature (°C) | | |
|---|---|---|---|---|---|---|---|---|---|
| Rarotonga, Cook Islands | 0.0 | 0.3 | 0.3 | 0.3 | 0.8 | 0.9 | 0.3 | 0.6 | 0.8 |
| Pohnpei, Federated States of Micronesia | -0.1 | 0.1 | 1.1 | 0.3 | 0.3 | 0.6 | 0.1 | 0.2 | 0.2 |
| Nadi, Fiji | 0.1 | 0.2 | 0.2 | 0.3 | 0.7 | 0.7 | 0.5 | 0.7 | 0.8 |
| Majuro, Marshall Islands | -0.7 | -0.2 | 0.2 | 0.3 | 0.4 | 0.4 | 0.2 | 0.3 | 0.3 |
| Apia, Samoa | -0.1 | 0.1 | 0.1 | 0.3 | 0.4 | 0.4 | 0.2 | 0.4 | 0.5 |
| Honiara, Solomon Islands | 0.0 | 0.5 | 0.6 | 0.1 | 0.2 | 0.4 | 0.2 | 0.3 | 0.5 |
| Lamap, Vanuatu | 0.2 | 0.3 | 0.9 | 0.4 | 0.7 | 0.9 | 0.2 | 0.5 | 0.5 |

**Table 7.2:** Change in statistically downscaled rainfall statistics projected for seven locations in the Pacific between 1981–2000 and 2021–2040. The statistical downscaling projections are driven by output from the dynamically downscaled ECHAM5/MPI-OM model under an A2 (high) emissions scenario.

| Location | Season | Mean rainfall (mm per day) 1981–2000[a] | Percent of rain days 1981–2000 | Change in percentage of rain days | Change in rainfall (mm per day) | | | |
|---|---|---|---|---|---|---|---|---|
| | | | | | On rain days only | | Overall average change | CCAM (ECHAM5/ MPI-OM) |
| | | | | | Median | 90th pctl | | |
| Rarotonga, Cook Islands* | Oct-Mar | 4.4 | 45 | 6 | 0.3 | 6.2 | 0.3 | 0.0 |
| | Apr-Sep | 3.6 | 39 | 5 | 0.1 | -3.1 | 0.2 | -0.1 |
| | All | 4.0 | 42 | 5 | 0.2 | 1.6 | 0.3 | 0.0 |
| Pohnpei, Federated States of Micronesia* | Oct-Mar | 11.8 | 81 | 4 | -0.1 | 0.3 | 0.2 | -0.5 |
| | Apr-Sep | 13.9 | 85 | 4 | -0.3 | 0.4 | 0.1 | -0.6 |
| | All | 12.8 | 83 | 4 | -0.2 | 0.3 | 0.1 | -0.5 |
| Nadi, Fiji* | Oct-Mar | 6.7 | 46 | -1 | 0.6 | 1.2 | 0.3 | 0.0 |
| | Apr-Sep | 2.6 | 24 | -1 | 0.3 | 0.6 | 0.1 | -0.1 |
| | All | 4.6 | 35 | -1 | 0.5 | 0.9 | 0.2 | 0.0 |
| Majuro, Marshall Islands | Oct-Mar | 8.8 | 73 | 3 | -0.3 | -0.7 | -0.1 | -0.5 |
| | Apr-Sep | 9.5 | 79 | 2 | -0.5 | -1.4 | -0.3 | -0.2 |
| | All | 9.1 | 76 | 2 | -0.4 | -1.0 | -0.2 | -0.3 |
| Apia, Samoa | Oct-Mar | 7.5 | 53 | 0 | -0.3 | -0.7 | -0.1 | 0.0 |
| | Apr-Sep | 4.3 | 39 | 0 | -0.2 | -1.1 | -0.1 | -0.1 |
| | All | 6.0 | 46 | 0 | -0.2 | -0.9 | -0.1 | 0.0 |
| Honiara, Solomon Islands* | Oct-Mar | 5.1 | 42 | -1 | 0.0 | -1.8 | -0.1 | -0.5 |
| | Apr-Sep | 3.0 | 37 | -1 | 0.0 | -1.1 | 0.0 | -0.6 |
| | All | 4.0 | 39 | -1 | 0.0 | -1.5 | 0.0 | -0.5 |
| Lamap, Vanuatu* | Oct-Mar | 8.0 | 63 | 2 | 0.4 | 2.0 | 0.4 | -0.1 |
| | Apr-Sep | 4.9 | 51 | 2 | 0.4 | 1.8 | 0.3 | -0.3 |
| | All | 6.5 | 57 | 2 | 0.4 | 1.9 | 0.3 | -0.2 |

[a] where observed data are available during reference period

* Statistically significant different trends observed between the climate station and dynamically downscaled data

In terms of temperature, a consistent pattern of warming is projected at all locations, ranging between 0.1 and 0.5°C by 2021–2040 (Tables 7.3 a,b). Generally, the increases projected by statistical downscaling are slightly less than those predicted from the dynamically downscaled ECHAM5/MPI-OM model. As noted in the tables there are some significant differences between the observed climate at a particular station location and the dynamically downscaled climate over a comparable period. These differences in climatic means as well as trends result in the differences in the projections between the statistical and dynamic approaches.

The statistically downscaled results are partly influenced by the observed trend (within the data used to train the statistical model), which includes both global warming trends and changes in natural variability, as well as other effects not necessarily captured by the downscaled simulations. The dynamically downscaled results, while including long-term effects of global warming, may not accurately capture all the local synoptic changes occurring and this may result in the divergence between trends over the historical period.

Hence, some of the differences between the dynamically and statistically downscaled results may be the result of the relative importance of localised changes and how consistent they are with broader regional and global anthropogenic change (Timm and Diaz, 2009). This is an area of further research.

The projected increase in minimum temperatures appears greater than maximum temperatures in most locations (Tables 7.3 a,b). The pattern of warming for both maximum and minimum temperatures is greatest for both the 10th percentile and median temperatures and less so for the 90th percentile temperatures. This is consistent with predictions derived directly from both global climate models and dynamical downscaling.

Table 7.3a: Change in statistically downscaled maximum temperature statistics projected for seven locations in the Pacific between 1981–2000 and 2021–2040. The statistical downscaling projections are driven by output from the dynamically downscaled ECHAM5 model under an A2 (high) emissions scenario.

| Location | Season | Mean maximum temperature (°C) 1981–2000 | Change in maximum temperature (°C) | | | CCAM (ECHAM5): change in mean temperature (°C) |
|---|---|---|---|---|---|---|
| | | | 10th percentile | Median | 90th percentile | |
| Rarotonga, Cook Islands* | Oct-Mar | 28.8 | 0.4 | 0.3 | 0.4 | 0.5 |
| | Apr-Sep | 26.8 | 0.3 | 0.3 | 0.4 | 0.5 |
| | All | 27.8 | 0.3 | 0.3 | 0.4 | 0.5 |
| Pohnpei, Federated States of Micronesia* | Oct-Mar | 31.2 | 0.5 | 0.2 | 0.3 | 0.4 |
| | Apr-Sep | 31.8 | 0.4 | 0.4 | 0.3 | 0.5 |
| | All | 31.5 | 0.4 | 0.3 | 0.3 | 0.4 |
| Nadi, Fiji | Oct-Mar | 31.1 | 0.4 | 0.3 | 0.2 | 0.5 |
| | Apr-Sep | 29.5 | 0.4 | 0.3 | 0.2 | 0.5 |
| | All | 30.3 | 0.4 | 0.3 | 0.2 | 0.5 |
| Majuro, Marshall Islands | Oct-Mar | 30.3 | 0.2 | 0.3 | 0.3 | 0.4 |
| | Apr-Sep | 30.6 | 0.3 | 0.3 | 0.3 | 0.4 |
| | All | 30.4 | 0.3 | 0.3 | 0.3 | 0.4 |
| Apia, Samoa* | Oct-Mar | 30.6 | 0.3 | 0.3 | 0.2 | 0.5 |
| | Apr-Sep | 30.1 | 0.3 | 0.2 | 0.2 | 0.5 |
| | All | 30.3 | 0.3 | 0.3 | 0.2 | 0.5 |
| Honiara, Solomon Islands* | Oct-Mar | 31.1 | 0.3 | 0.1 | 0.1 | 0.4 |
| | Apr-Sep | 30.8 | 0.2 | 0.1 | 0.1 | 0.5 |
| | All | 31.0 | 0.3 | 0.1 | 0.1 | 0.4 |
| Lamap, Vanuatu* | Oct-Mar | 30.1 | 0.4 | 0.4 | 0.4 | 0.6 |
| | Apr-Sep | 28.6 | 0.5 | 0.5 | 0.5 | 0.7 |
| | All | 29.4 | 0.5 | 0.4 | 0.5 | 0.6 |

* Statistically significant different trends observed between the climate station and dynamically downscaled data

**Table 7.3b:** Change in statistically downscaled minimum temperature statistics projected for seven locations in the Pacific between 1981–2000 and 2021–2040. The statistical downscaling projections are driven by output from the dynamically downscaled ECHAM5 model under the A2 (high) emissions scenario.

| Location | Season | Mean minimum temperature (°C) 1981–2000 | Change in minimum temperature (°C) | | | CCAM (ECHAM5): change in mean temperature (°C) |
|---|---|---|---|---|---|---|
| | | | 10th percentile | Median | 90th percentile | |
| Rarotonga, Cook Islands* | Oct-Mar | 22.9 | 0.5 | 0.3 | 0.2 | 0.5 |
| | Apr-Sep | 20.8 | 0.4 | 0.3 | 0.2 | 0.5 |
| | All | 21.9 | 0.4 | 0.3 | 0.2 | 0.5 |
| Pohnpei, Micronesia* | Oct-Mar | 23.7 | 0.2 | 0.1 | 0.2 | 0.4 |
| | Apr-Sep | 23.3 | 0.0 | 0.1 | 0.0 | 0.5 |
| | All | 23.5 | 0.1 | 0.1 | 0.0 | 0.4 |
| Nadi, Fiji* | Oct-Mar | 22.8 | 0.6 | 0.5 | 0.1 | 0.5 |
| | Apr-Sep | 20.7 | 0.6 | 0.5 | 0.3 | 0.5 |
| | All | 21.7 | 0.6 | 0.5 | 0.2 | 0.5 |
| Majuro, Marshall Islands* | Oct-Mar | 26.0 | 0.1 | 0.4 | 0.2 | 0.4 |
| | Apr-Sep | 25.7 | 0.2 | 0.1 | 0.2 | 0.4 |
| | All | 25.8 | 0.2 | 0.3 | 0.2 | 0.4 |
| Apia, Samoa | Oct-Mar | 24.3 | 0.2 | 0.2 | 0.0 | 0.5 |
| | Apr-Sep | 23.7 | 0.1 | 0.1 | 0.0 | 0.5 |
| | All | 24.0 | 0.2 | 0.2 | 0.0 | 0.5 |
| Honiara, Solomon Islands | Oct-Mar | 23.1 | 0.1 | 0.2 | 0.4 | 0.4 |
| | Apr-Sep | 22.6 | 0.2 | 0.2 | 0.0 | 0.5 |
| | All | 22.9 | 0.2 | 0.2 | 0.1 | 0.4 |
| Lamap, Vanuatu* | Oct-Mar | 22.9 | 0.4 | 0.2 | 0.1 | 0.6 |
| | Apr-Sep | 22.2 | 0.5 | 0.3 | 0.2 | 0.7 |
| | All | 22.5 | 0.4 | 0.2 | 0.2 | 0.6 |

* Statistically significant different trends observed between the climate station and dynamically downscaled data

Time series information has also been generated as part of the statistical downscaling activities for the 17 locations (Table 4.3). An example has been provided of some monthly statistics for Lamap in Vanuatu (Figure 7.18). The figure shows that there is, as expected, strong within-season variation and interannual variation of the data as well as a slightly increasing rate over time of the upward trend of some variables. There is also a slight increase projected over time of the variation of median monthly rainfall on rain days.

## 7.3.2 Statistical Downscaling Summary

Statistical downscaling projections are somewhat different to those based upon global and dynamically downscaled models. In part, this is a result of the statistical model being based upon both observed local trends and large-scale dynamically downscaled outputs. In addition, statistical downscaling is designed to deliver information at a given station, and thus takes into consideration local influences on climate and weather.

Dynamical models produce information across a grid of varying resolution and thus may not account for all these local effects. The differences between dynamical and statistically derived projections are being examined and are the basis of future research.

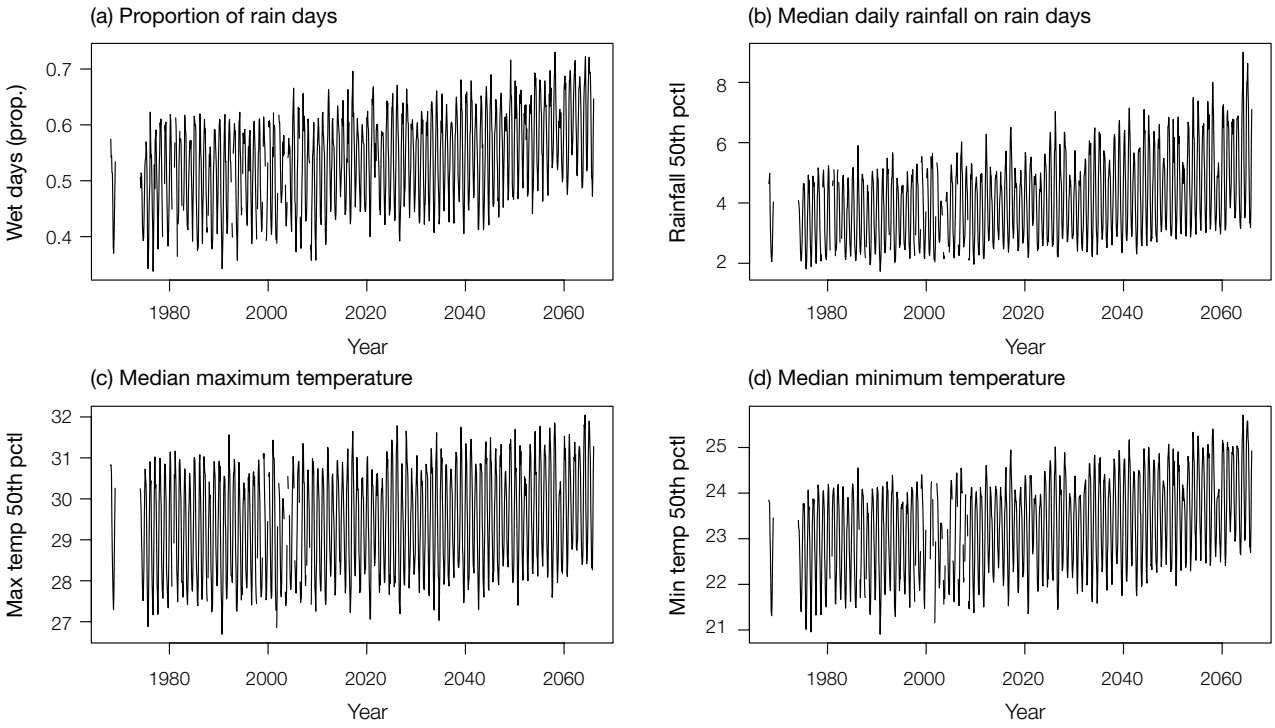


**Figure 7.18:** Statistically downscaled time series projections to 2065 for Lamap, Vanuatu. The statistical downscaling projections are driven by output from the dynamically downscaled ECHAM5/MPI-OM model under an A2 (high) emissions scenario.

# 7.4 Tropical cyclone projections

## 7.4.1 Introduction

Tropical cyclones are among the most destructive weather phenomena on Earth. The associated strong winds coupled with heavy rainfall and possible storm surges often have devastating consequences for life and property in various tropical regions of the world. In the tropical Pacific, small island developing States such as those in the PCCSP region are very vulnerable to catastrophic impacts of tropical cyclones. Determining realistic future changes in tropical cyclone activity (such as frequency and intensity) is therefore important for these areas. However, projection of realistic future changes in tropical cyclone activity at a regional spatial scale is still an unresolved issue; partly due to large variations in modelling results (Knutson et al., 2010) and partly due to model deficiencies in representing the large-scale environmental conditions that are known to influence tropical cyclones, including patterns of variability such as the El Niño-Southern Oscillation and large-scale climate features such as the South Pacific Convergence Zone (Brown et al., 2011).

Despite the global climate models' inadequacies in representing regional scales, the reproduction of current climate of tropical cyclones on larger scales was shown in Chapter 5 to be quite promising, due to the use of the multiple projection methods. These results provide some confidence in the projections of future changes in tropical cyclone frequency for the PCCSP region. Here the projected change in tropical cyclone frequency is defined in terms of the percentage change between the current climate (1980–1999) and the future climate for the A2 (high) scenario (2080–2099).

At the global scale, modelling studies consistently project a decrease in mean tropical cyclone frequency ranging from 6 to 34% by the late 21st century (Knutson et al., 2010). This decrease is more robust in the Southern Hemisphere than in the Northern Hemisphere, and may be due to a combination of increased vertical wind shear in the Southern Hemisphere, and smaller increases in sea-surface temperature compared with the Northern Hemisphere.

In individual basins, projected 21st century changes are highly variable, with both increases and decreases in frequency of more than 50%. Theory and high-resolution modelling also suggest that climate change may lead to an increase in cyclone intensity by about 2–11%.

In an attempt to provide more specific projections of tropical cyclone frequency for individual countries, the PCCSP region is divided into three sub-basins. These are the south-west basin (0–40ºS; 130–170ºE), the south-east basin (0–40ºS; 170ºE-130ºW) and the north basin (0–15ºN; 130–180ºE). The results of the cyclone frequency projections for the three basins from the different methods described in Section 4.8 are presented in Table 7.4 and Figure 7.19 (for a subset of the models and methods). Projected changes in cyclone intensity are also described. Changes in wind risk hazard are evaluated for the study region by applying the Tropical Cyclone Risk Model to tracks of tropical cyclone-like vortices detected in downscaled global climate models.

**Table 7.4:** Projected percentage change in tropical cyclone frequency between the current climate (1980–1999) and the late 21st century (2080–2099). Blue (red) shading indicates a statistically significant decrease (increase) in projected tropical cyclone frequency at the 95% confidence interval. Blue (red) numbers indicate projected decreases (increases) in tropical cyclone frequency that are not statistically significant. CCAM refers to the 60 km dynamically downscaled simulations. The CVP, CDD and GPI methods are described in Section 4.8. Significance level testing is not available for the GPI method.

| Model | South-east basin | | | | South-west basin | | | | North basin | | | |
|---|---|---|---|---|---|---|---|---|---|---|---|---|
| | Projection method | | | | | | | | | | | |
| | CCAM | CVP | CDD | GPI | CCAM | CVP | CDD | GPI | CCAM | CVP | CDD | GPI |
| CSIRO-Mk3.5 | -65 | +10 | +10 | -60 | -45 | +50 | +20 | -70 | 0 | +10 | 0 | -80 |
| ECHAM5/MPI-OM | -50 | -20 | +25 | -35 | -80 | -30 | +15 | -25 | -80 | -25 | +5 | -30 |
| GFDL-CM2.0 | -70 | | -30 | -20 | -60 | | -35 | -5 | -45 | | 0 | +5 |
| GFDL-CM2.1 | -50 | -10 | -30 | -25 | -70 | -20 | -25 | -5 | -50 | -10 | -30 | -5 |
| MIROC3.2 (medres) | -90 | | | -75 | -80 | | | -85 | -50 | | | -85 |
| UKMO-HadCM3 | -55 | | | -30 | -55 | | | +10 | -30 | | | +15 |
| BCCR-BCM2.0 | | | -90 | -5 | | | -90 | +10 | | | -100 | +15 |
| CGCM3.1 | | | +30 | -20 | | | +30 | -10 | | | -5 | -10 |
| CNRM-CM3 | | | -20 | -35 | | | +10 | -20 | | | -5 | -30 |
| MRI-CGCM2.3.2 | | | 0 | -25 | | | -15 | -5 | | | 0 | 0 |
| CSIRO-Mk3.0 | | | | -50 | | | | -55 | | | | -65 |
| UKMO-HadGEM1 | | | | -5 | | | | +5 | | | | +15 |
| IPSL-CM4 | | | | -20 | | | | -15 | | | | -20 |
| ECHO-G | | | | -35 | | | | -25 | | | | -25 |
| ENSEMBLE | -60 | -6 | -13 | -30 | -65 | 0 | -11 | -20 | -45 | -5 | -17 | -20 |

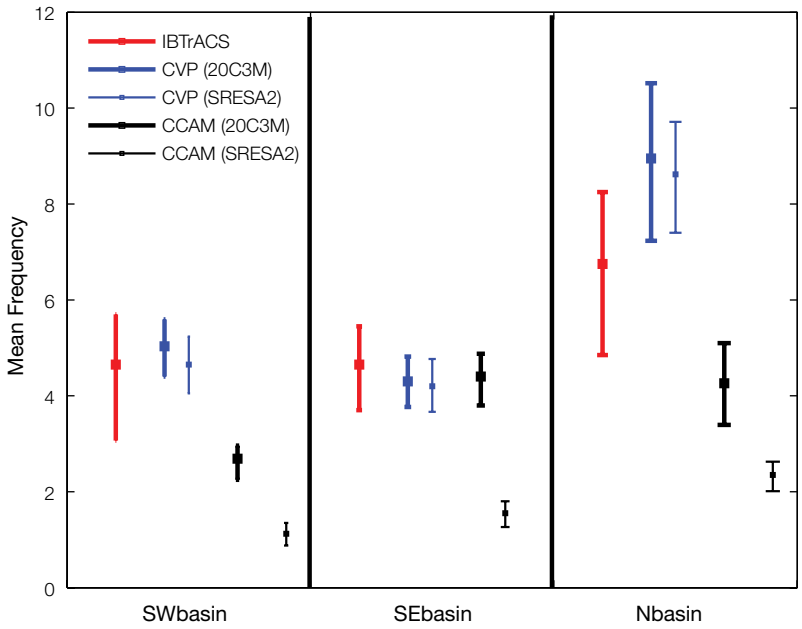


**Figure 7.19:** Average of all models of the late 21st century projected annual tropical cyclone frequency for the three sub-basins of the PCCSP region using the CCAM downscaling technique (thin black) and the Curvature Vorticity Parameter (CVP) method (thin blue). Also shown are the annual cyclone frequencies for the current climate for the CCAM downscaling technique (thick black) and the CVP method (thick blue). Red lines indicate observed mean tropical cyclone frequency. Bars denote 95% confidence interval. A change is considered likely if there is no overlap between current and future climate bars. Results are based on outputs from the CSIRO-Mk3.5, ECHAM5/MPI-OM, GFDL-CM2.0 and GFDL-CM2.1 global climate models (CVP) and CCAM simulations based on these global models.

## 7.4.2 Tropical Cyclone Frequency Projections in Downscaled Models

Overall, the CCAM results project a likely decrease in tropical cyclone frequency for all three sub-basins by the late 21st century (Figure 7.19). These decreases in frequency range from 50–70% for the south-east basin, 45–80% for the south-west basin and 0–80% for the north basin (Table 7.4).

In the south-east basin, the decrease in the CCAM multi-model average cyclone frequency as determined by the CSIRO Direct Detection technique, is clearly evident when comparing Figures 7.20a and 7.20b, with greatest decrease in the longitude band of 170–180ºE (Figures 7.20c, 7.20d), and near the latitude of 15ºS. Similarly, the greatest projected decrease in frequency for the south-west basin occurs mainly in the Coral Sea region (15ºS; 150–170ºE), where tropical cyclones are frequently spawned. For the north basin, the projected decrease occurs mainly in the region 10ºN; 130–150ºE (Figure 7.20e).

The location of cyclone genesis is just one component in the cyclone risk for a region. The risk for a region is also determined by the track, duration and intensity of storms traversing the region. The changes in cyclone numbers and days from the six CCAM simulations have been calculated (not shown). Most models show a small increase in the number of tropical cyclones occurring south of 20°S although there is little consistency between the models in the spatial pattern of the projected change. The change in intensity is discussed in detail later in this chapter.

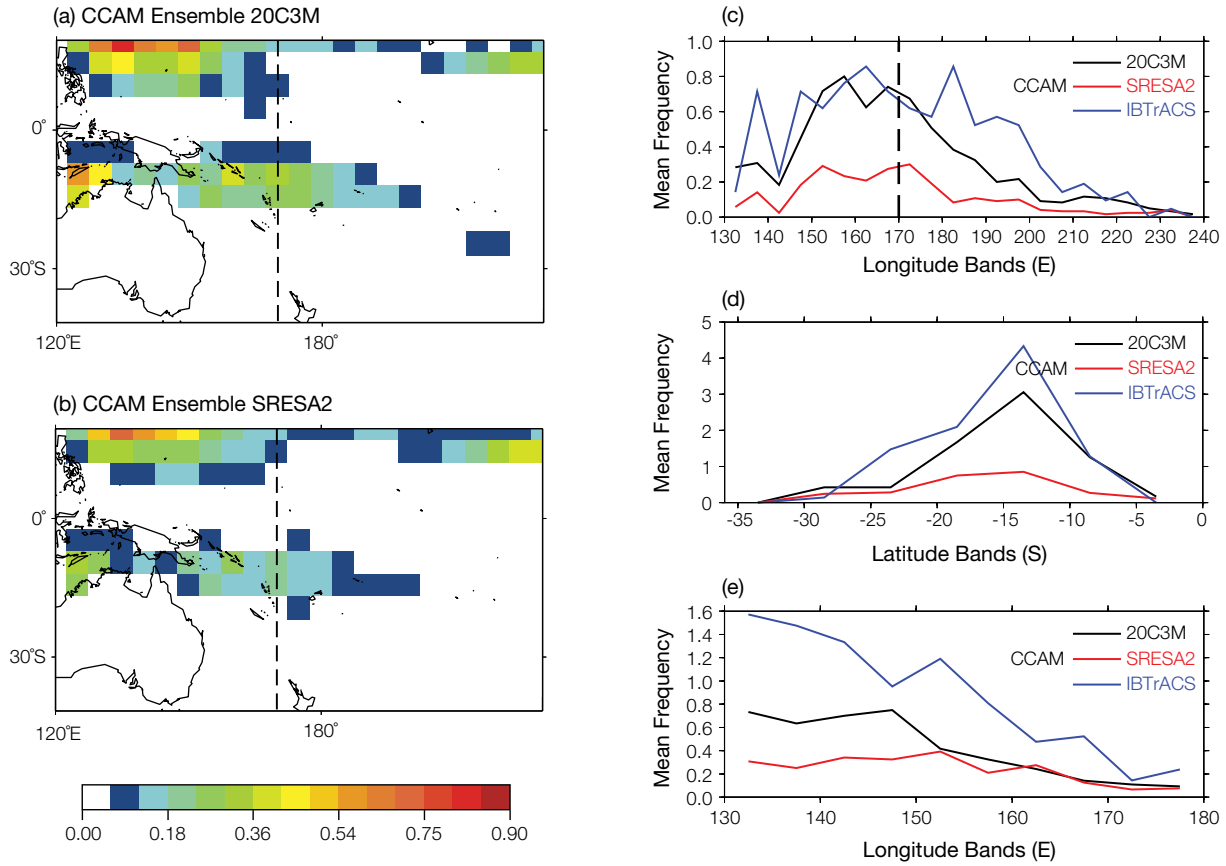


**Figure 7.20:** Multi-model mean distribution of tropical cyclone frequency (in 5º × 5º boxes) obtained using the CSIRO Direct Detection technique applied to the 65 km CCAM model for (a) current climate, (1980–1999, labelled 20C3m) and (b) late 21st century using the A2 high emissions scenario (2080–2099, labelled SRESA2). Cyclone frequency distributions are also shown in 5º (c) longitudinal and (d) latitudinal bands for the South Pacific and (e) longitudinal band for the north-west Pacific south of 20ºN. The dashed line at 170ºE in (c) separates the eastern and western basins of the South Pacific.

## 7.4.3 Cyclone Frequency Projections in Global Climate Models

In general, the Curvature Vorticity Parameter (CVP) approach discussed in Section 4.8 is based on output from three global climate models. It projects a small decrease in tropical cyclone frequency for the PCCSP region by the late 21st century (Figure 7.19). In the south-east basin, the projected change ranges from a 20% decrease for the ECHAM5/MPI-OM model to a 10% increase for the CSIRO-Mk3.5 model (Table 7.4). However, these changes are not statistically significant at the 95% level. The spatial distribution of tropical cyclone formation locations determined by taking the multi-model mean of the three global models shows no substantial change between the current (Figure 7.21a) and future (Figure 7.21b) distributions.

For the south-west basin, two global climate models (GFDL-CM2.1 and ECHAM5/MPI-OM) project a decrease in tropical cyclone numbers by about 20–30%. The CSIRO-Mk3.5 model, on the other hand, projects a likely increase of about 50%. A small decrease in tropical cyclone numbers is also projected for the north basin. However, this decrease is not statistically significant at the 95% level.

On average, the CSIRO Direct Detection (CDD) method discussed in Section 4.8 projects a multi-model average decrease in tropical cyclone genesis frequency for the PCCSP region by the late 21st century (Table 7.4 and Figure 7.22). However, there is little confidence in this projected change for the southern Pacific as in both the south-east basin and in the south-west basin, four out of eight models project a likely increase in tropical cyclone frequency and four out of eight models project a likely decrease in tropical cyclone frequency. In the northern basin there is greater confidence in the change as only one model projects a likely increase in tropical cyclone frequency.

## 7.4.4 Cyclone Frequency Projections from the Genesis Potential Index

The Genesis Potential Index (GPI) methodology has the advantage that more models (14) can be considered in the development of projections for changes in cyclone frequency.

The GPI method projects decreases of between 20% and 30% for the three basins (Figure 7.23). In the south-east basin, all models project a decrease in frequency with projected changes ranging from 5% to 70%. In the south-west basin, 11 out of 14 models project a decrease in the frequency with projected changes ranging from an increase of 10% to a decrease of 85%. In the north basin, the changes range from an increase of 15% to a decrease of 80%. Ten out of 14 models project a decrease in frequency for this basin.

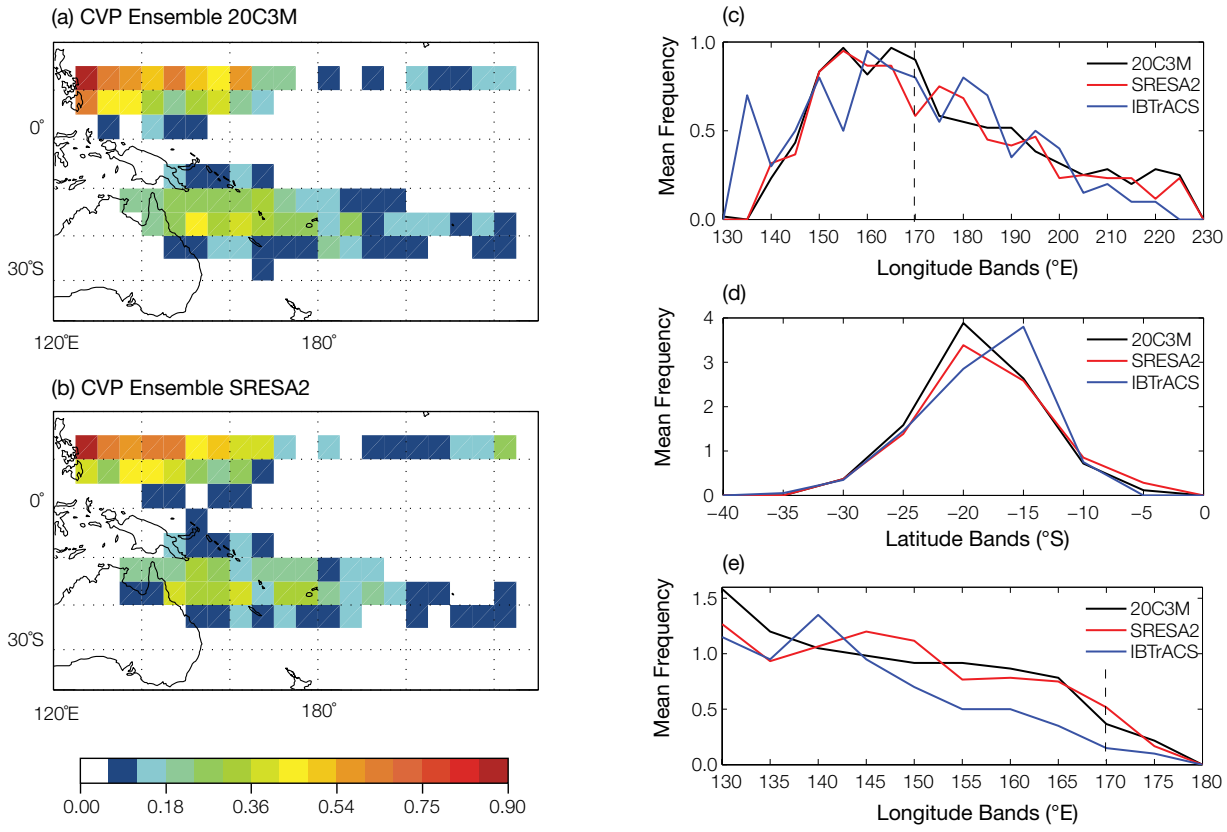


**Figure 7.21:** Multi-model mean distribution of tropical cyclone frequency (in 5° × 5° boxes) obtained using the CVP approach for (a) current climate (labelled 20C3m) and (b) late 21st century using the A2 (high) emissions scenario (labelled SRESA2). Cyclone frequency distributions are also shown in 5° (c) longitudinal and (d) latitudinal bands for the South Pacific and (e) longitudinal band for the north-west Pacific south of 20°N. The dashed line at 170°E in (c) separates the eastern and western basins of the South Pacific.

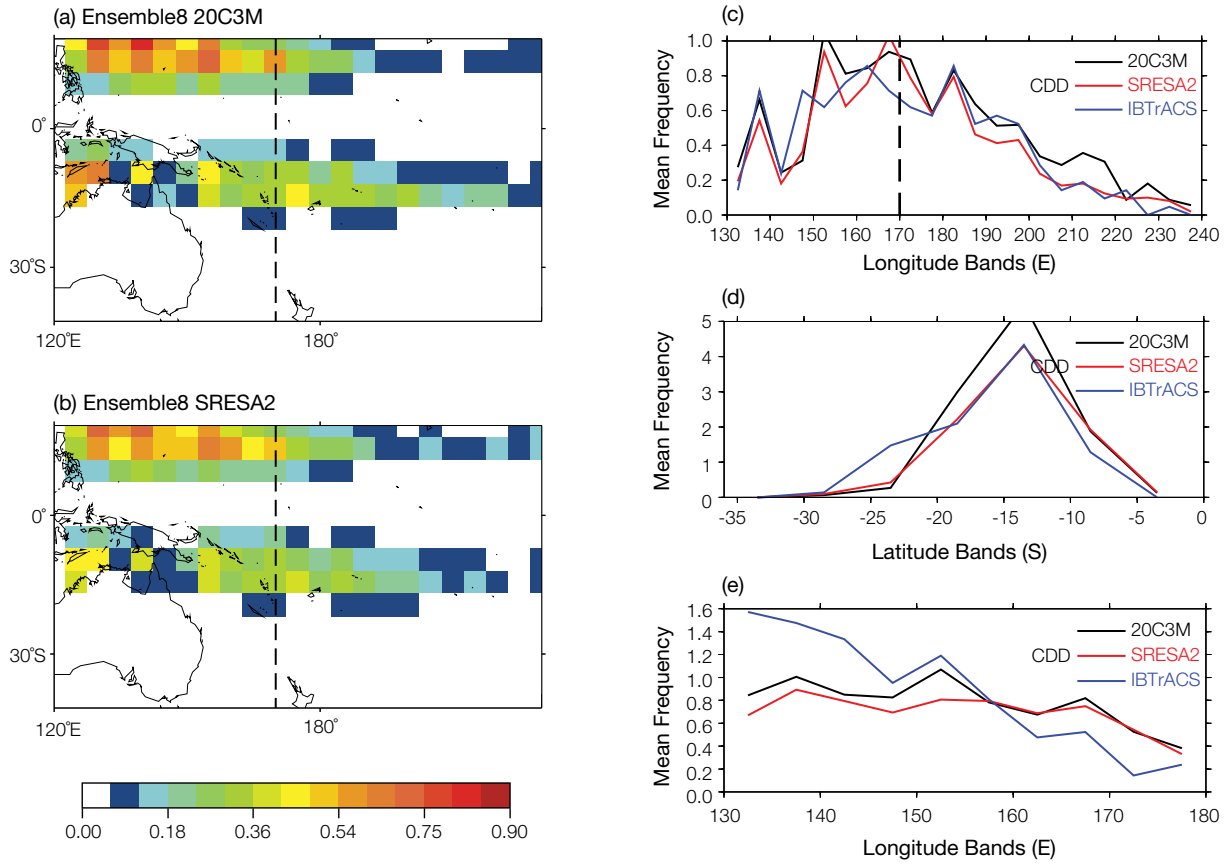


**Figure 7.22:** Multi-model mean distribution of tropical cyclone frequency (in 5° × 5° boxes) obtained using the CDD method on global climate model data for (a) current climate (labelled 20C3m) and (b) late 21st century using the A2 (high) emissions scenario (labelled SRESA2). Cyclone frequency distributions are also shown in 5° (c) longitudinal and (d) latitudinal bands for the South Pacific and (e) longitudinal band for the north-west Pacific south of 20°N. The dashed line at 170°E in (c) separates the eastern and western basins of the South Pacific.

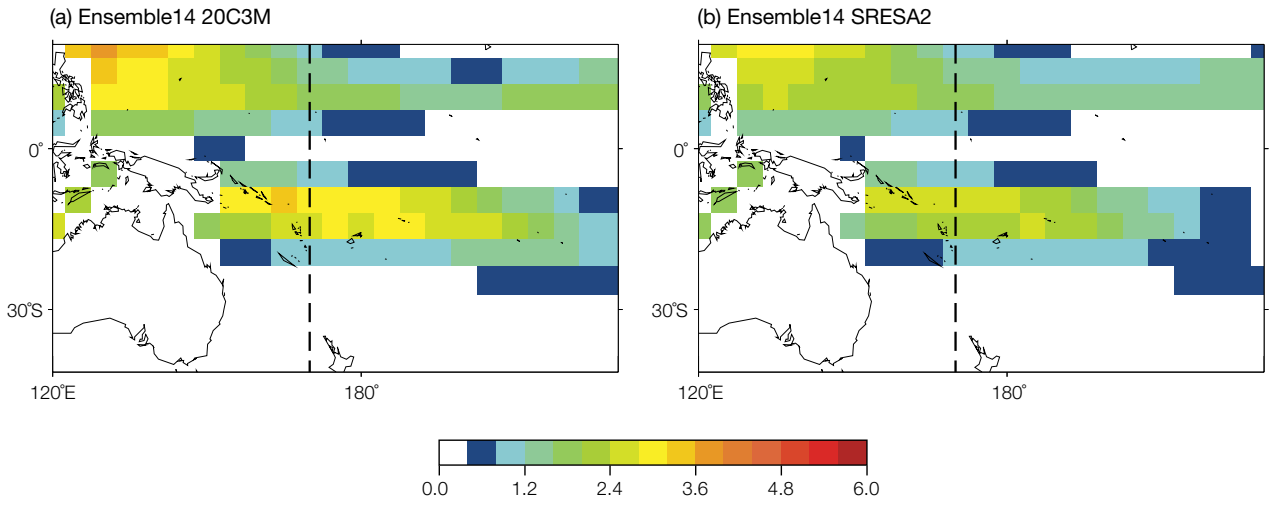


**Figure 7.23:** Multi-model mean distribution of tropical cyclone frequency (in 5° × 5° boxes) obtained using the GPI method for (a) current climate (labelled 20C3m) and (b) late 21st century using the A2 (high) emissions scenario (labelled SRESA2).

## 7.4.5 Cyclone Intensity Projections

The development of projections for changes in cyclone intensity requires that features such as the bands of heavy precipitation that accompany a cyclone and the eye wall (the zone of high winds that causes damage) are resolved by a model. However, these features occur at a spatial scale smaller than can be resolved by either global or regional climate models and thus the development of projections of changes in tropical cyclone intensity is difficult. However, a number of research groups have attempted to provide such projections and the results of those studies that are applicable to the South Pacific are summarised in Table 7.5. Note that the A1B, not the A2 emissions scenario, has been used here.

The PCCSP has used three methods to estimate projected changes in intensity. The first of these uses the Maximum Potential Intensity (MPI) component of the GPI, the second method uses the storm maximum wind speed simulated in the cyclone-like vortices detected in the CCAM simulations, and the third method scales the CCAM projections for use in the Tropical Cyclone Risk Model. The results using the MPI method are summarised in Table 7.6. In this analysis no attempt has been made to provide basin-specific projections – the projected changes apply to the full PCCSP study region.

Most models project a decrease in the MPI across the PCCSP region. The projected decrease is largest in the models that project the greatest decrease in the frequency. Models that project either a moderate decrease or slight increase in frequency also project small increases in the MPI.

**Table 7.5:** A summary of the projections of tropical cyclone intensity in the South Pacific, extracted from global modelling studies for a warmer climate under the A1B (medium) emissions scenarios or a three times carbon dioxide concentration. Bold text in the Technique column indicates type of analysis used. The projections of changes are in either the average intensity or the maximum intensity of cyclones in the South Pacific. In the far right column, projected decreases in frequency are in bold. (Adapted from Knutson et al., 2010).

| **Tropical cyclone intensity changes (%)** | **Model** | **Technique** | **Emissions scenario** | **Measure of cyclone intensity** | **Projection time period** | **Change in maximum wind speed in the South Pacific** (percentage change or frequency change, as noted) |
|---|---|---|---|---|---|---|
| Vecchi and Soden, (2007a) | CMIP3 18-model | Potential Intensity calculations from the output of global models<br>**Statistical downscaling** | A1B | Max wind speed | 100yr trend | + 1% |
| Emanuel et al. (2008) | CMIP3 7-model | **Statistical downscaling** | A1B | Max wind speed | 2181–2200 minus 1981–2000 | -1% |
| Oouchi et al. (2006) | MRI/JMA time slice experiment with global model TL959 L60 (~20km) | **Dynamical downscaling** | A1B | Average intensity (wind speed) | 1982–1993 minus 2080–2099 | -2% |
| Oouchi et al. (2006) | MRI/JMA time slice experiment with global model TL959 L60 (~20km) | **Dynamical downscaling** | A1B | Average annual maximum intensity (wind speed) | 1982–1993 minus 2080–2099 | -22% |
| Walsh et al. (2004) | Australia CSIRO DARLAM regional model | **Dynamical downscaling** | $3xCO_2$ | Central pressure | 2061–2090 minus 1961–1990 | **+26%**<br>**P<970 mb** |
| Leslie et al. (2007) | USA OU-CGCM with high-res. window. | **Dynamical downscaling** | IPCC estimated $CO_2$ from 1970–1999, and IS92a increasing concentration from 2000–2050 | Wind speed | 2000 to 2050 control and IS92a (6 members) | **+100% #>30m/s by 2050** |

The results based on the storm maximum wind speed from the cyclone-like vortices detected in the CCAM simulations are presented in Figure 7.24. This analysis includes calculations of the proportion of storms in the late 21st century climate (2080–2099) that are stronger than the current climate 50th percentile, 75th percentile and 90th percentile wind speeds and the proportion of storms that are weaker than the 25th and 10th percentile wind speeds. If the proportion of storms in the late 21st century lies above the current climate curve, then there is an increase in the proportion of storms that are stronger (or weaker) than in the current climate. The analysis has been conducted for the north basin and the southern Pacific (south-east basin and south-west basin combined) and shows different behaviour in intensity changes for the two basins. In the north basin, only one CCAM simulation (based on CSIRO-Mk3.5) projects an increase in the proportion of storms that will occur in the stronger categories. Most simulations project an increase in the proportion of storms occurring in the weaker categories.

In the southern Pacific, five of the six simulations show an increase in the proportion of the most severe storms (those stronger than the current climate 90th percentile storm maximum wind speed). The latitude of maximum intensity in the southern Pacific is projected to move south by 5° of latitude from approximately 18°S in the current climate to approximately 23°S in the late 21st century.

The results of Figure 7.24 are consistent with finer resolution modelling studies such as those of Bender et al. (2011). They show that models that are able to realistically simulate the intensity of cyclones show an increase in the proportion of storms occurring in the strongest categories. These results should, however, be used with caution. The resolution of the models considered in this analysis is not fine enough to quantify changes in the intensity of tropical cyclones. Projections of changes in tropical cyclone intensity require the use of specialised models that are run with horizontal grid spacing of 5 km or less.

**Table 7.6:** Projected changes in GPI for each of the sub-basins and projected changes in Maximum Potential Intensity (MPI) for the PCCSP region for the late 21st century using the A2 (high) emissions scenario.

| | GPI change | | | MPI change (%) |
|---|---|---|---|---|
| **Model** | **SW** | **SE** | **N** | |
| CSIRO-Mk3.5 | -60 | -70 | -80 | -59 |
| ECHAM5/MPI-OM | -35 | -25 | -30 | -13 |
| GFDL-CM2.0 | -20 | -5 | +5 | 1 |
| GFDL-CM2.1 | -25 | -5 | -5 | 1 |
| MIROC3.2 (medres) | -75 | -85 | -85 | -50 |
| UKMO-HadCM3 | -30 | +10 | +15 | 5 |
| BCCR-BCM2.0 | -5 | +10 | +15 | 6 |
| CGCM3.1 | -20 | -10 | -10 | -9 |
| CNRM-CM3 | -35 | -20 | -30 | -5 |
| MRI-CGCM2.3.2 | -25 | -5 | 0 | -2 |
| CSIRO-Mk3.0 | -50 | -55 | -65 | -37 |
| UKMO-HadGEM1 | -5 | +5 | +15 | 13 |
| IPSL-CM4 | -20 | -15 | -20 | -10 |
| ECHO-G | -35 | -25 | -25 | -7 |

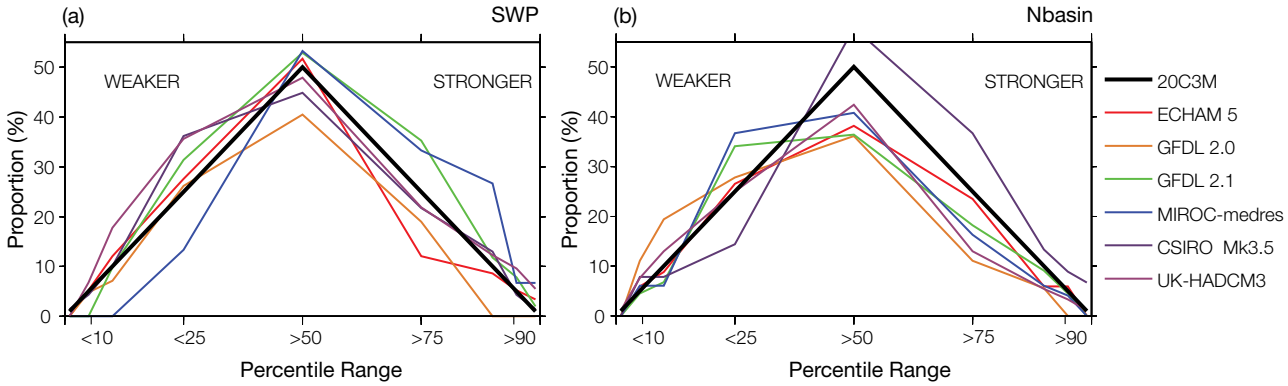


**Figure 7.24:** The proportion of projected storms in the late 21st century climate (2080–2099) that are stronger than the current climate (1980–1999) 50th percentile, 75th percentile and 90th percentile wind speeds and the proportion of storms that are weaker than the 25th and 10th percentile wind speeds in the CCAM simulations for (a) the southern Pacific and (b) the north basin.

## 7.4.6 Cyclonic Wind Hazard Projections

The Tropical Cyclone Risk Model used tracks of tropical cyclone-like vortices detected in the CCAM model as proxies for tropical cyclones. These were then used in the Tropical Cyclone Risk Model to produce estimates of the cyclonic wind hazard for both the current climate and late 21st century for the South Pacific (130°E–150°W, 30°S–0°) and the north-west Pacific (130°E–180°, 0°-15°N).

As described earlier and in Chapter 5, the CCAM simulations produce storms that are both less frequent and less intense than the real world. To overcome this, the frequency and intensity of the current climate simulations were re-scaled to match the historical record. This scaling was then held fixed for each future climate simulation. The resulting change in wind hazard between the current and future climate reflects the combined effect of changes to the frequency, intensity and track locations of the tropical cyclone-like vortices.

Maps of the relative change in the 500-year return period wind hazard between the current climate and the 20-year period centred on 2090 were created for each simulation. There is not a high degree of consistency between the spatial patterns of the projected change in wind hazard between the six simulations. This is illustrated by Figure 7.25, which shows the projected hazard change for the GFDL-CM2.1 and CSIRO-Mk3.5-based simulations. There were, however, some common trends shown in each of the model simulations. For the South Pacific, most models indicate a reduction in cyclonic wind hazard north of latitude 20ºS and some regions of increased hazard south of latitude 20ºS. Note, however, that the spatial patterns of these regions of increased wind hazard differs between models (c.f. Figures 7.25a and 7.25c). This increase in wind hazard coincides with the projected increase in the number of tropical cyclones occurring south of 20°S that was noted earlier. Similar increases have previously been found in the modelling study of Leslie et al. (2007). The poleward shift in cyclone frequency was found to also coincide with a poleward shift in the more intense storms. For the North Pacific region (between the equator and 15°N), there is a general reduction in cyclonic wind hazard between the current and future climate simulations as a result of a decrease in storm frequency close to the equator.

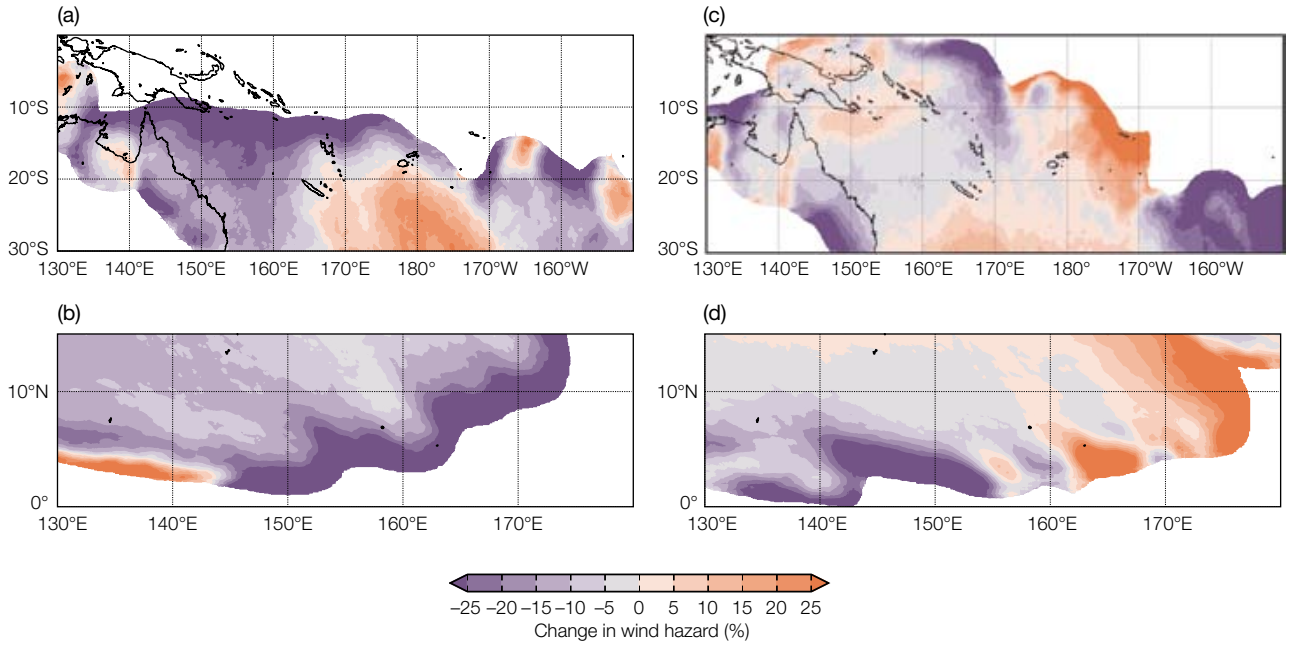


**Figure 7.25:** Percentage change in 500-year return period cyclonic wind speeds projected for the South Pacific (a and c) and the north-west Pacific (b and d) based on GFDL-CM2.1 (a and b) and CSIRO-Mk3.5 (c and d) for the late 21st century using the A2 (high) emissions scenario.

# 7.5 Downscaling Summary

The CCAM 60 km downscaled projections for the PCCSP region are broadly consistent with those of the global climate models presented in Chapter 6. However, some differences between global models and CCAM projections are noted, such as bands of rainfall decrease around latitudes 8°N and 8°S. These projections are also supported by the additional downscaling results using a variety of other regional climate models. The CCAM 8 km downscaled projections show regional-scale variations of the climate change signal, largely related to the topography of the Pacific Islands. Statistical downscaling shows slightly less warming, more consistent with the observed trends.

Projections of changes in tropical cyclone frequency based upon CMIP3 global climate models and CCAM show a number of important differences. The analysis of the global models using the CVP and CDD techniques shows that they are able to reproduce the climatology of tropical cyclones for the current climate. However, when these techniques are applied to the outputs from these models to provide projections of changes in frequency for the late 21st century, there is considerable variability in the projected changes between both the global models and the two techniques. Similarly, application of the GPI technique to the global model outputs also shows considerable variability between the models in projected changes in the occurrence of tropical cyclones affecting the study region.

In contrast, when the CDD technique is applied to CCAM outputs the projected changes show little variability between the six simulations considered. This may be due to the use of a single modelling system for the downscaled runs analysed. Importantly, the CCAM simulations underestimate the occurrence of tropical cyclones occurring east of 180°E. This deficiency should be considered when using tropical cyclone projections based upon these simulations.

Projections based upon these different modelling systems and analysis techniques show that tropical cyclone frequency in the PCCSP region is likely to decrease by the late 21st century. There is a moderate level of confidence in this projection, with little consistency found in the magnitude of the projected changes between either the models or the analysis methods.

Most simulations project an increase in the proportion of the most severe storms in the south-west Pacific and a southward movement in the latitude at which maximum intensity occurs. In the northern basin, most simulations project an increase in the proportion of storms occurring in the weaker categories. For the South Pacific, most models indicate a reduction in cyclonic wind hazard north of 20°S and regions of increased wind hazard south of 20°S. This coincides with the projected increase in the number of tropical cyclones occurring south of 20°S and with a poleward shift in the latitude at which storms are most intense. For the North Pacific region, there is a general reduction in cyclonic wind hazard between the current and future climate simulations as a result of a decrease in storm frequency close to the equator.